SEARCH FOR A DECONFINED QUARK GLUON PHASE OF STRONGLY INTERACTING MATTER IN $\bar{p}$-p INTERACTIONS AT $\sqrt{s} \simeq 2$ TeV

Submitted by Scientists at Purdue University
and the Fermi National Accelerator Laboratory

Abstract

We propose to use a double arm magnetic spectrometer and a central tracking chamber located at the DØ intersection area that can utilize low, from 10^{27} to $10^{28}cm^{-2}sec^{-1}$, luminosity to measure the transverse momentum distributions dN/dp_t up to p_t = 1.0 GeV/c for centrally produced $p^{\pm},\pi^{\pm},e^{\pm}$ as a function of the charged particle multiplicity n_c. The temperature T and the size of centrally produced plasma can be extracted from the transverse momentum (p_t) distributions dN/dp_t and from the like pion correlations, respectively.

Evidence for a quark gluon plasma manifests itself by

(a) Breaks in $\langle p_t \rangle$ as a function of dn_c/dy in the central region $|y| \leq 1$.
(b) Changes in the particle composition as a function of the charged particle multiplicity n_c.
(c) Onset of low mass dilepton pair production as a function of the charged particle multiplicity n_c.

We also propose to measure the ratio of the gamma-ray multiplicity n_γ to charged particle multiplicity n_c for high multiplicity events. Evidence for a Centauro event, if produced in the central region, would manifest itself by high charged particle multiplicities $n_c \simeq 30$ with the number of n_γ consistent with zero.

Because we momentum analyze only low energy particles in observing these signatures, the size and complexity of this apparatus is one tenth of that required for a 4π detector which studies high transverse momentum reactions.

Person to contact: L. J. Gutay
Commercial phone: (317) 494-5047
FTS phone: 331-2084

Names of the Experimenters

Members of Purdue University:

Professors:	D. D. Carmony
	A. S. Hirsch
	L. J. Gutay
	N. T. Porile
	R. P. Scharenberg
	B. C. Stringfellow
Research Associates:	A. Bujak
	Z. Seres
Students:	C. Sangster
	F. Poole

Members of Fermi National Accelerator Laboratory:

Physicist:	F. Turkot

I. Introduction

Although the original models for particle production were statistical and thermodynamic in nature (Fermi[1] and Landau[2]), the main thrust of high energy physics has been the study of particles and resonances. The fact that these have definite quantum numbers and could be classified into various representations of symmetry groups by Gell-Mann[3] as well as the existence of Bjorken scaling[4] has led to the hypothesis that hadrons are made of quarks and gluons.

The absence of any evidence for the existence of free quarks has led to the concept of quark confinement. From the concept of asymptotic freedom[5] QCD evolved[6] as the theory of strong interactions in agreement with numerous hard scattering experiments. Lattice gauge calculations of QCD predict a phase transition from hadrons to a quark-gluon plasma at sufficiently high temperatures and/or quark densities.[7] There is a general theoretical concensus that temperatures of $T \sim 200$ MeV and/or quark antiquark densities of $n_q + \bar{n}_q = 2$ to 4 per cubic fermi are required to produce a quark-gluon plasma.[8] Such a density may be thought of as two protons being "placed on top of each other."

There are strong experimental indications from the CERN UA1[9] collaboration that such temperatures may be produced in high multiplicity collisions at $\sqrt{s} = 0.54$ TeV. Evidence for thermalization at lower temperature $T = 120$ MeV suggests that it is likely that temperatures $T > 200$ MeV (see Section II) and quark densities $\gtrsim 2$ to 4 per cubic fermi (see Appendix I) are attainable in high multiplicity $n_c > 50$ collisions at $\sqrt{s} = 2$ TeV.

The energy density vs. T for a phase transition[10] from SU_2 lattice gauge calculations is shown in Fig. 1 for a gluon plasma. Similar results have been obtained from lattice gauge calculations using SU_3 color fields.[11] To cast Fig. 1 into a form that can be related to experimental quantities we divide the y axis of Fig. 1 by T. The general shape remains unchanged as shown in Fig. 2 where we introduced the symbol $\sigma = \frac{\varepsilon}{T}$, the entropy density. According to statistical mechanics and thermodynamics, the entropy density is proportional to the rate of particle production over a unit rapidity ($\sigma \propto \frac{dn}{dy}$) and the temperature is proportional to the average transverse

momentum ($T \propto \langle p_t \rangle$). Thus from the above relations and Fig. 2 we can deduce the shape of dn/dy as a function of $\langle p_t \rangle$ as shown in Fig. 3. As discussed in the next section (II), it is possible to quantitatively calibrate $\langle p_t \rangle$ versus T so that the critical (deconfinement) temperature could be determined. That means dn_c/dp_t for pions must be a Bose-Einstein distribution in the range $p_t \leq 1.0$ GeV/c. Then it should be possible to speak of a thermalized energy density.

From the study of high transverse energy jets, Bjorken[8] concluded that energy densities well above the expected phase transition energy densities may exist, already at the CERN $\bar{p}$-p collider energies.

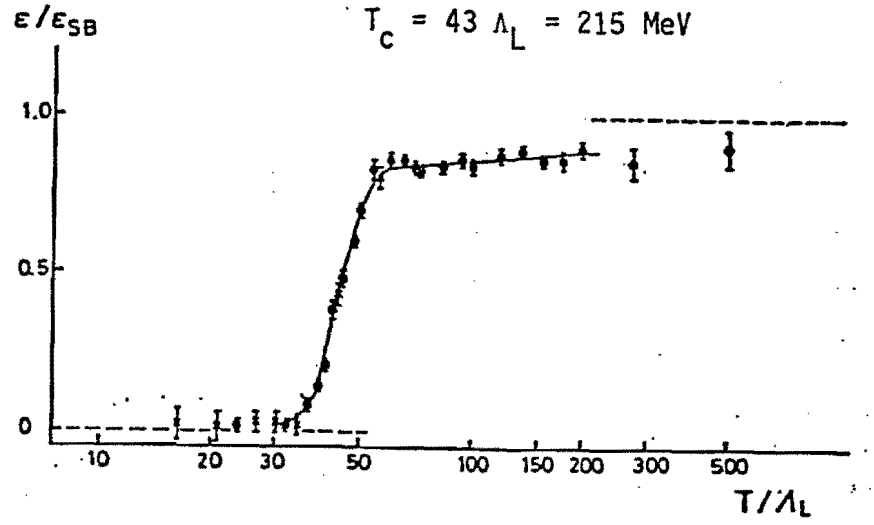

Fig. 1. Theoretical prediction for the energy density as function of temperature for a gluon plasma from Ref. 10. (Sharpness enhanced by log plot.)

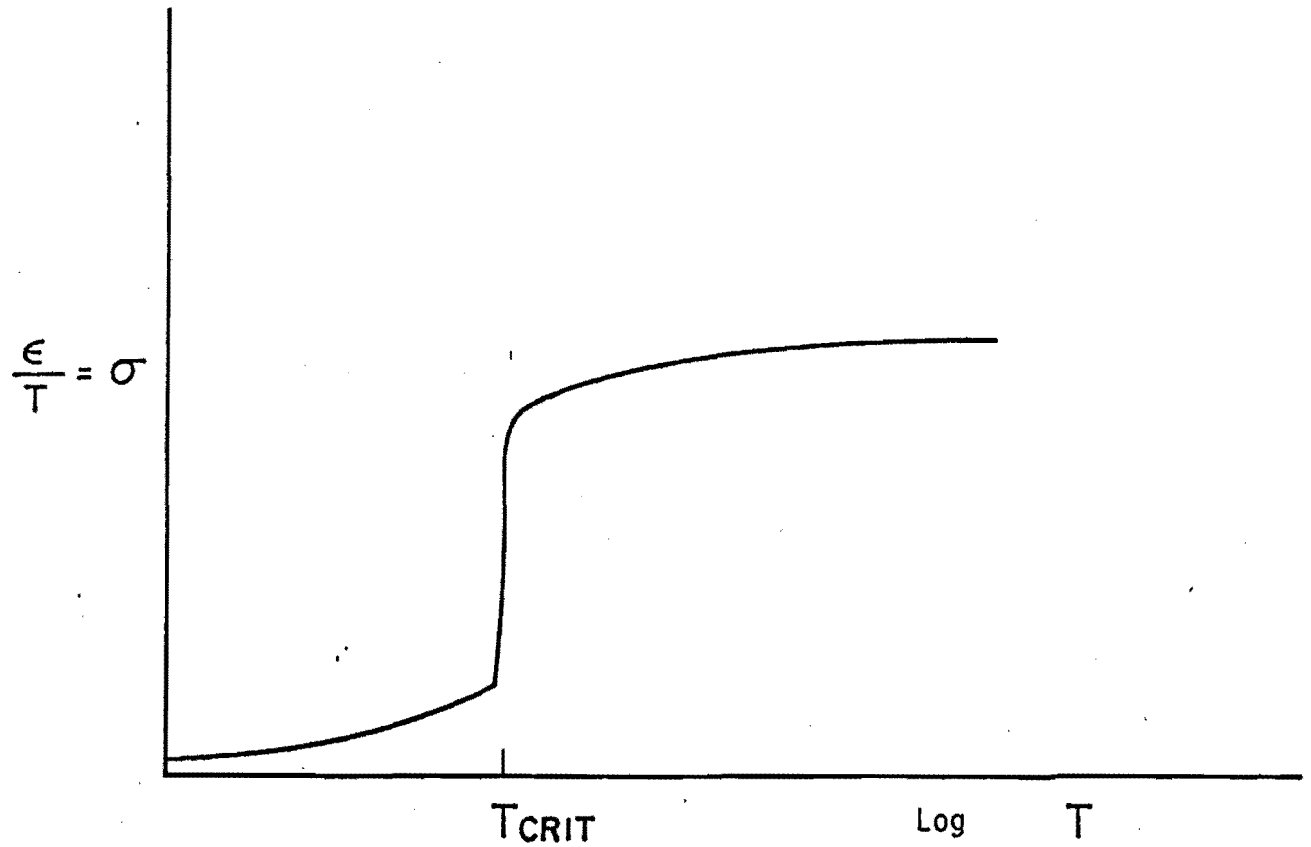

Fig. 2. Theoretical prediction for the entropy density as function of temperature for a gluon plasma from Ref. 10.

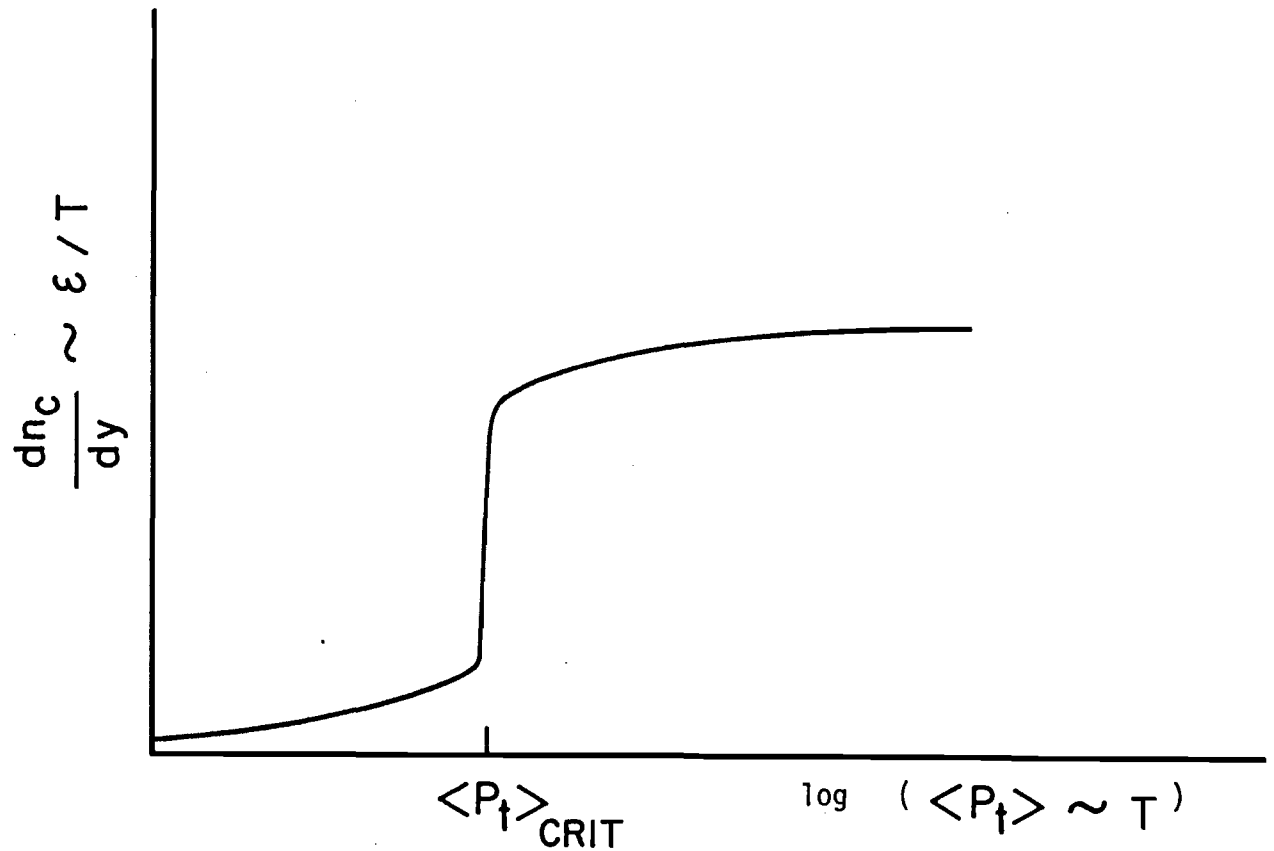

Fig. 3. Theoretical expectation of the dependence of the average transverse multiplicity on particle density in the rapidity space.

II. Motivation for the Experiment

A. Hadrons Emerging from the Quark-Gluon Plasma

To study the central region of $\bar{p}p$ collisions in the DØ area of the Fermi National Accelerator Laboratory at a center of mass energy of 2 TeV, we propose using a pair of low momentum magnetic spectrometers with particle identification. We will measure the transverse momentum (p_t) distribution of centrally produced $p^{\pm}, k^{\pm}, \pi^{\pm}, e^{\pm}$, for $p_t < 1.0$ GeV/c as a function of the charged multiplicity $n_c = \int (dn_c/dy)/dy$.

It has been observed[12] at the CERN $\bar{p}p$ collider ($\sqrt{s} = 0.54$ TeV) that the number of charged particles in the central region is larger than those observed at ISR energies, and that there exists a clear dependence of $\langle p_t \rangle$ in the central region on the central multiplicity n_c.[9]

It has been pointed out[8] that this increase in $\langle p_t \rangle$ as a function of n_c could indicate the combined effect of transverse expansion and temperature caused by the energy which has been deposited in the central region. The $\langle p_t \rangle$ versus particle multiplicity is shown in Fig. 4.

As seen in Fig. 4, the increase of $\langle p_t \rangle$ with dn/dy is the same at the CERN-collider, the ISR, and for fixed target Fermilab data for the common range of dn/dy. Figure 4 shows a cessation of the rise in $\langle p_t \rangle$ with increasing dn/dy which is compatible with a phase transition; that is, as the entropy density ($\varepsilon/T \propto dn/dy$) continues to increase the temperature ($T \propto \langle p_t \rangle$) remains constant. From data at a single $\sqrt{s}$ we cannot rule out that this is merely a kinematic effect. It is therefore important to repeat this measurement at $\sqrt{s} = 2$ TeV where the range of dn/dy is at least 1.5 times as great simply from the ln(s) effect. Since the CERN-collider experiments[22] have reported (Fig. 5) an excess of high multiplicity events as compared to a KNO scaling curve (or in comparison to ISR) the assumed $n_c \sim \ln(s)$ underestimates the available dn/dy range at Fermilab.

Our group has studied pion production in the central region[13] in pp collisions at $\sqrt{s} = 7.7$ GeV. The observed p_t distribution can be quantitatively interpreted in terms of a thermodynamic picture where the

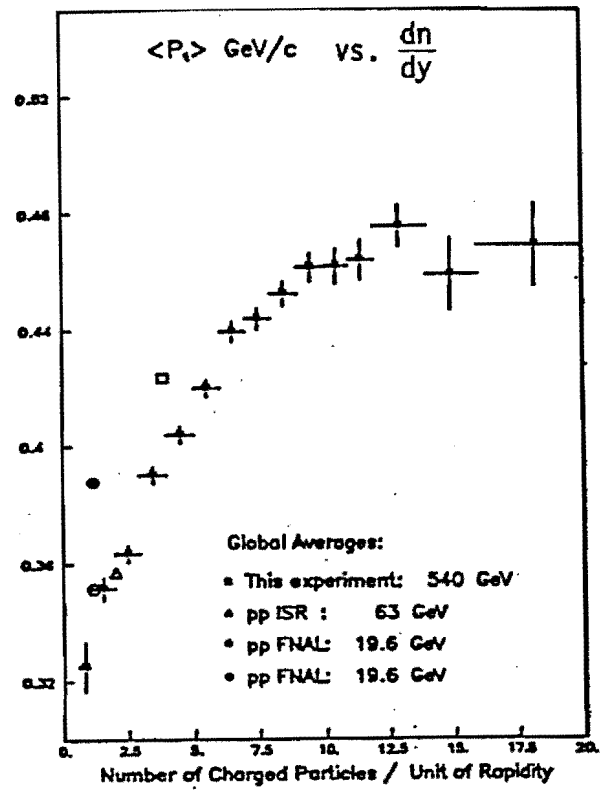

Fig. 4. The mean transverse momentum of charged hadrons ($\sqrt{s}$ = 540 GeV) as a function of charged track multiplicity in the rapidity interval $|y| < 2.5$. (Error bars are purely statistical.) From Ref. 9. To be compared with Fig. 3 (interchange x,y variables).

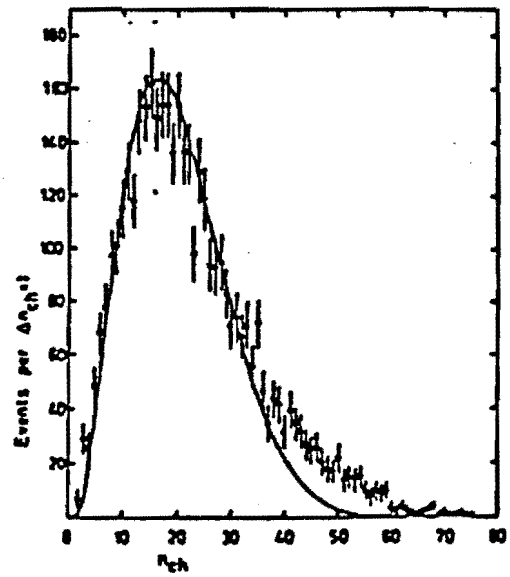

Fig. 5. The distribution of observed charged multiplicities in the UA5 experiment. Errors shown are statistical. The curve is a fit to lower energy data and scaled to $\sqrt{s}$ = 540 GeV. From Ref. 22.

distribution dn/dp_t yields a Bose-Einstein statistical distribution from which a temperature of 117 MeV can be extracted. The fit to the data is shown in Fig. 6. Other authors have found similar values for the temperature of nuclear matter at SLAC,[14] FNAL[15] and ISR[16] energies.

In our work,[13] the determination of T = 117 MeV involved 4, 6, 8 and 10 prong events. If we assume that $\bar{n}_c = 5$ for these events this corresponds to $\frac{d\bar{n}_c}{dy} \sim 1.3$. Accepting the thermodynamical relations, which hold outside the region of phase transition;

$$\frac{dn}{dy} \propto T^3$$

we can estimate the critical value of dn/dy as follows:

$$\frac{\left(\frac{dn_c}{dy}\right)_{crit}}{1.3} = \left(\frac{T_{crit}}{117}\right)^3 = \left(\frac{215}{117}\right)^3$$

From which we obtain

$$\left(\frac{dn_c}{dy}\right)_{crit} = 8$$

The subscripts "c" and "crit" denote charged and critical, respectively. We also made use of the theoretically predicted $T_{crit} = 215$ MeV.

An independent estimate of the energy density, ε, in the central region using a one dimensional model is given in Appendix I.

As shown in Fig. 4, the mean transverse momenty $\langle p_t \rangle$, at $\sqrt{s} = 0.54$ TeV has been measured as a function of dn_c/dy in the range 1 to 15 and indeed it is observed that $\langle p_t \rangle$ becomes a constant for $\frac{dnc}{dy} > 8$. This indicates that temperatures on the order of twice those attainable at $\sqrt{s} = 7.7$ GeV may just be reached at $\sqrt{s} \sim .5$ TeV. However, the experiment needs to be done at higher energies to rule out kinematic effects, i.e. lack of energy and with much higher statistics. The flattening of $\langle p_t \rangle$ has also been detected for very complex events by the Brazil-Japan cosmic ray collaboration.[17]

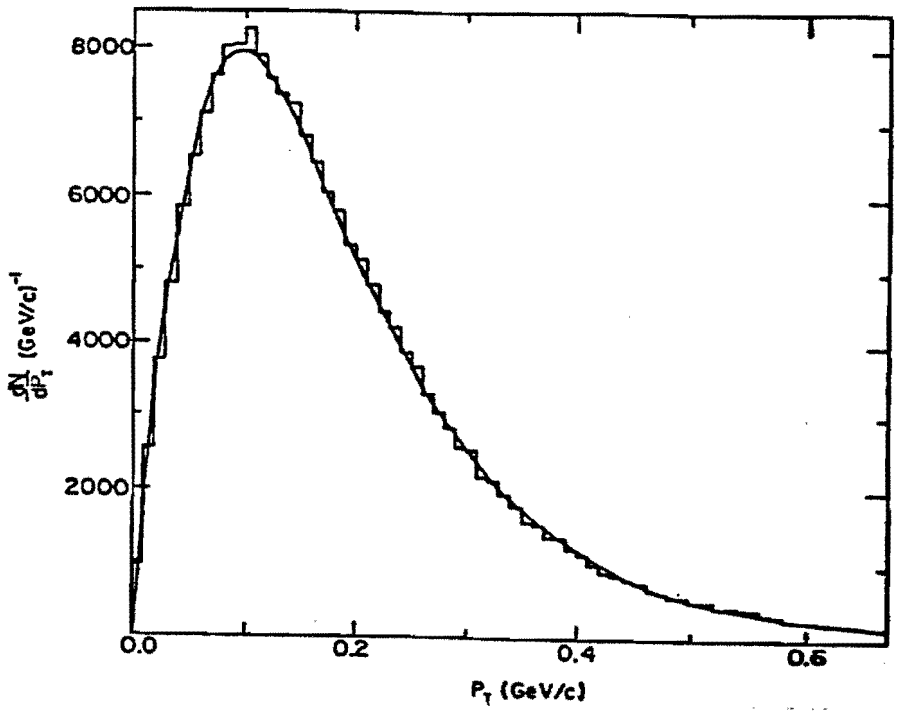

Fig. 6. The transverse-momentum distribution for central particles in the asymptotic large-multiplicity limit in the reaction $p_1 + p_2 \rightarrow p_3 + X$. The curve is a fit to the Bose-Einstein statistical distribution. From Ref. 13.

B. Dileptons Emerging from a Quark-Gluon Plasma

So far we have discussed how a quark-gluon plasma would manifest itself by emission of strongly interacting particles. An alternate signature would be the production of low mass lepton pairs. The mechanism is $\bar{q}q$ annihilation into leptons;

$$q + \bar{q} \rightarrow e^+ + e^- \quad .$$

The importance of this reaction for quark matter diagnostics has been discussed by Domokos.[18] The cross sections for dilepton pairs will be suppressed by α^2 compared to the strong interaction rates. A rough estimate that takes into account the thermal motion of quarks in the plasma by Domokos derives the temperature and invariant mass dependence of the dilepton production.[18] Using his formulae we estimate that the dilepton rate in 200 MeV < $m_{e^+e^-}$ < 600 MeV mass range is about 0.5 percent of the event rate for the $dn_c/dy = 25$ events with $T \sim 200$ MeV. They are expected to be isotropic in the rest frame of the plasma and have a low ($m_{e^+e^-}$ < 600 MeV) effective mass.

A competing process to $\bar{q}q < e^+e^-$ is the

$$\pi^+ + \pi^- \rightarrow e^+ + e^- \quad .$$

The relative rates are shown in Figs. 7a and 7b from Ref. 18.

Our double arm spectrometer is well suited for detecting e^+e^- pairs when they are produced with the thermal energy of $2T \approx 400$ MeV back to back. According to Ref. 18 the low mass (200 MeV < $m_{e^+e^-}$ < 600 MeV) is dominated by the $\bar{q}q \rightarrow e^+e^-$ process and the corresponding lepton momenta are such that both our hadron data can be collected concurrently with the dilepton events. The advantage of the dilepton channel is that they can be emitted by the plasma any time during its lifetime.

C. Centauro Events

The number of "unusual" events which may be observed at $\sqrt{s} = 2$ TeV can be estimated from cosmic ray data if it is assumed they are initiated by a $\bar{p}$-p collision.[17] A translation in terms of center of mass energies is shown in Fig. 8.

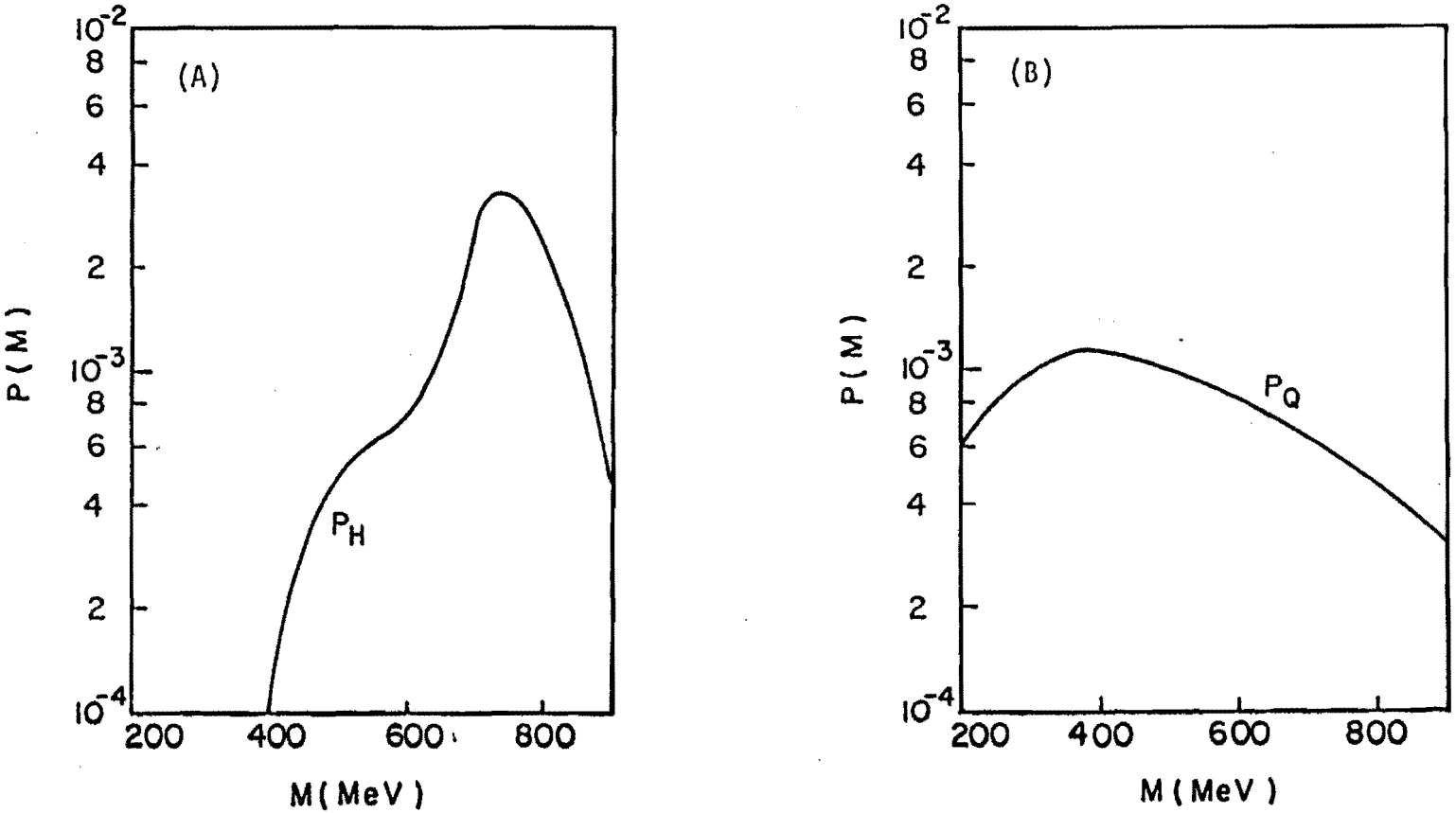

Fig. 7. Normalized dilepton roles for (A) $\pi^+ + \pi^- \rightarrow e^+ + e^-$ and (B) $\bar{q} + q \rightarrow e^+e^-$. Ref. 18.

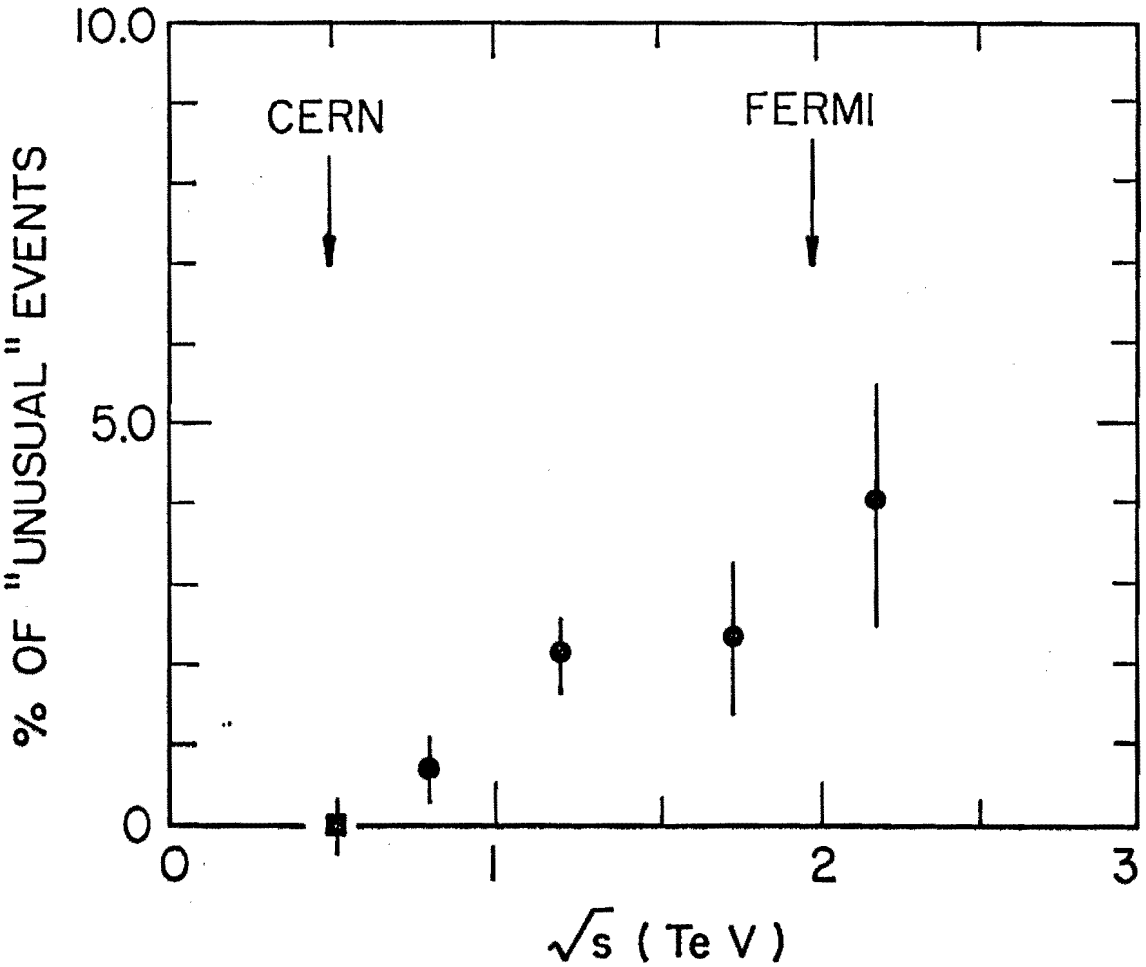

Fig. 8. The number of unusual events as function of the center of mass energy from Ref. 17.

These $\sqrt{s}$ values are somewhat uncertain because they depend on the estimates of the energy of the primary p-p collision. The signature of these Centauro events is characterized by a large number of hadrons $n_c \sim 75$ and a number of gamma rays n_γ consistent with zero. Thus it is possible to search for this type of event if we are also sensitive to the number n_γ, provided that the particles emerge in the central region. Since Centauro events have only been observed in cosmic ray experiments, both the interaction point and the dn/dy for these events are unknown as discussed in Ref. 19. If the decay product emerge dominantly in the central region we would measure about 30 charged hadrons with a number of n_γ consistent with zero. Any associated particles $|y| \leq 1$ would be observed in our charged particle spectrometer. We would expect that such a spectacular signature which could be due to dominant baryon-antibaryon production could be seen if these events were more numerous than the fluctuations of n_γ expected for the normal events which are dominated by pion production.

III. Experimental Layout

A. Central Region

The top view of the experimental apparatus is shown in Fig. 9a. In the central region $|y| \leq 3$ the n_c and n_γ multiplicities are determined by a five layer cylindrical proportional wire chamber CWPC, a cross section of which is shown in Fig. 10, and the end cap arrays. The details of the CWPC are presented in Appendix II. In the first level of reconstruction only the inner three layers of the wire chambers are used. The individual particles which have been observed in the magnetic spectrometers must arise from this vertex.

Since we are interested in events whose charged multiplicities are up to five times the average n_c, we must distinguish between a single high multiplicity interaction and the occurrence of two independent lower multiplicity events in the same collision pulse. Reconstruction of the vertex or vertices will allow us to resolve two different vertices which are more than one cm apart along the beam direction. For a collision pulse width FWHM of 50 cm this means we can reduce this accidental background by a factor of 50. At low ($10^{27}cm^{-2}sec^{-1}$) luminosities accidentals are not a problem. At high luminosities ($10^{29}cm^{-2}sec^{-1}$) reconstruction of the event is an essential feature.

The fourth and fifth outer layers of the CWPC are used to detect the gammas (n_γ) converted in the lead and to give a crude photon direction. Since $n_\gamma \sim n_c$ we should get an excellent indication that for these events $\langle n_\gamma \rangle \sim \langle n_c \rangle$. Apertures in the converter are provided so that low momentum particles can be seen by the magnetic spectrometers. Of course only for non-Centauro events is it expected that $n_\gamma \sim n_c$.

The dimensions of the low momentum spectrometers are shown in Fig. 9b. The traditional design has a pseudorapidity acceptance of $|y| \leq 1$ and an azimuthal range $\Delta\phi$ which assures that about one particle is detected when the multiplicity is $n_c = 35$. The magnetic gaps are 75 inches long, 10 inches and 5 inches deep as seen from the interaction region. The double gap magnet, which is detailed in Appendix III has copper coils and an iron return path. The five cylindrical chambers determine the incident particle direction θ_1, three drift chambers behind the magnet the final

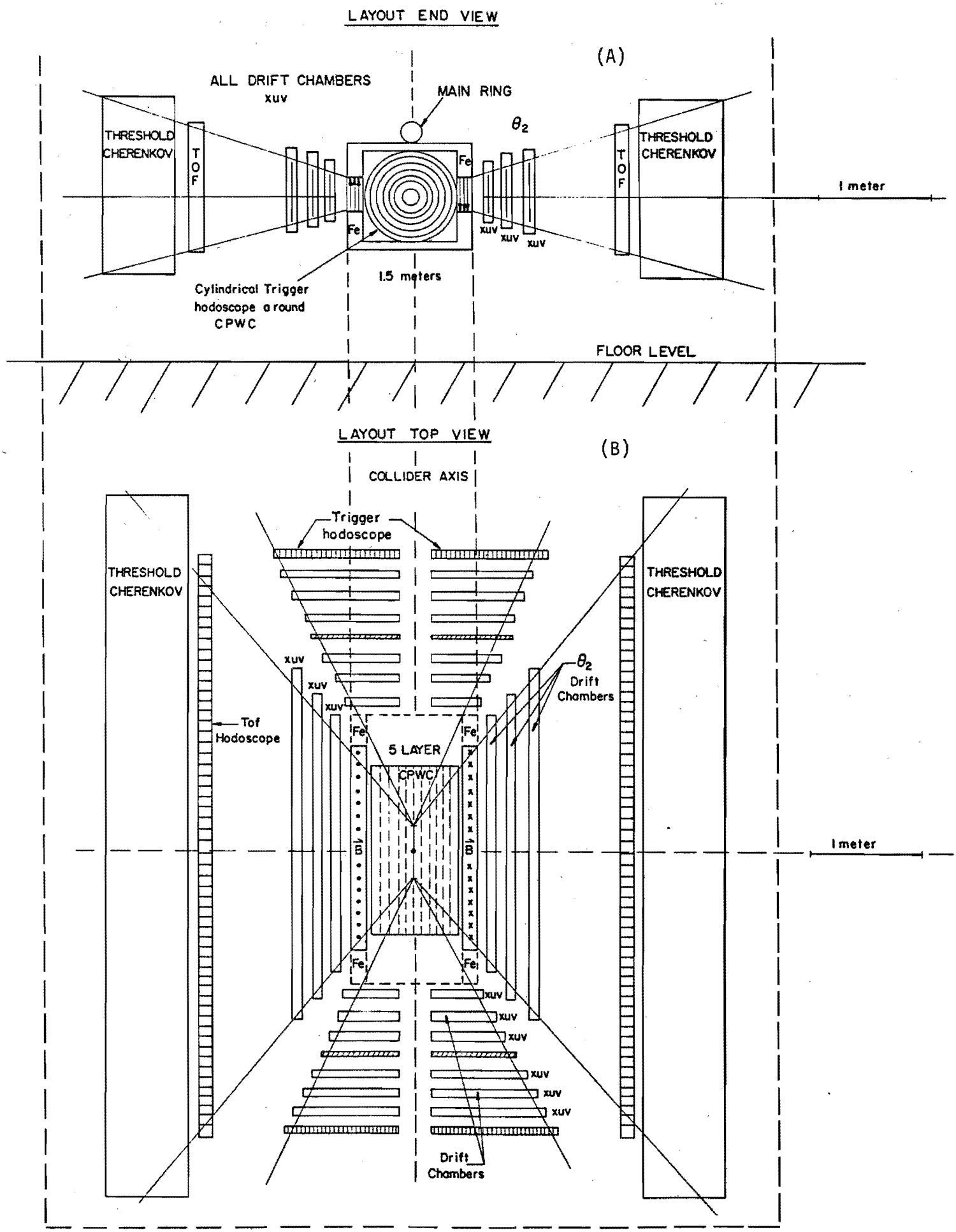

Fig. 9. Layout of the experimental apparatus; (A) end view and (b) top view.

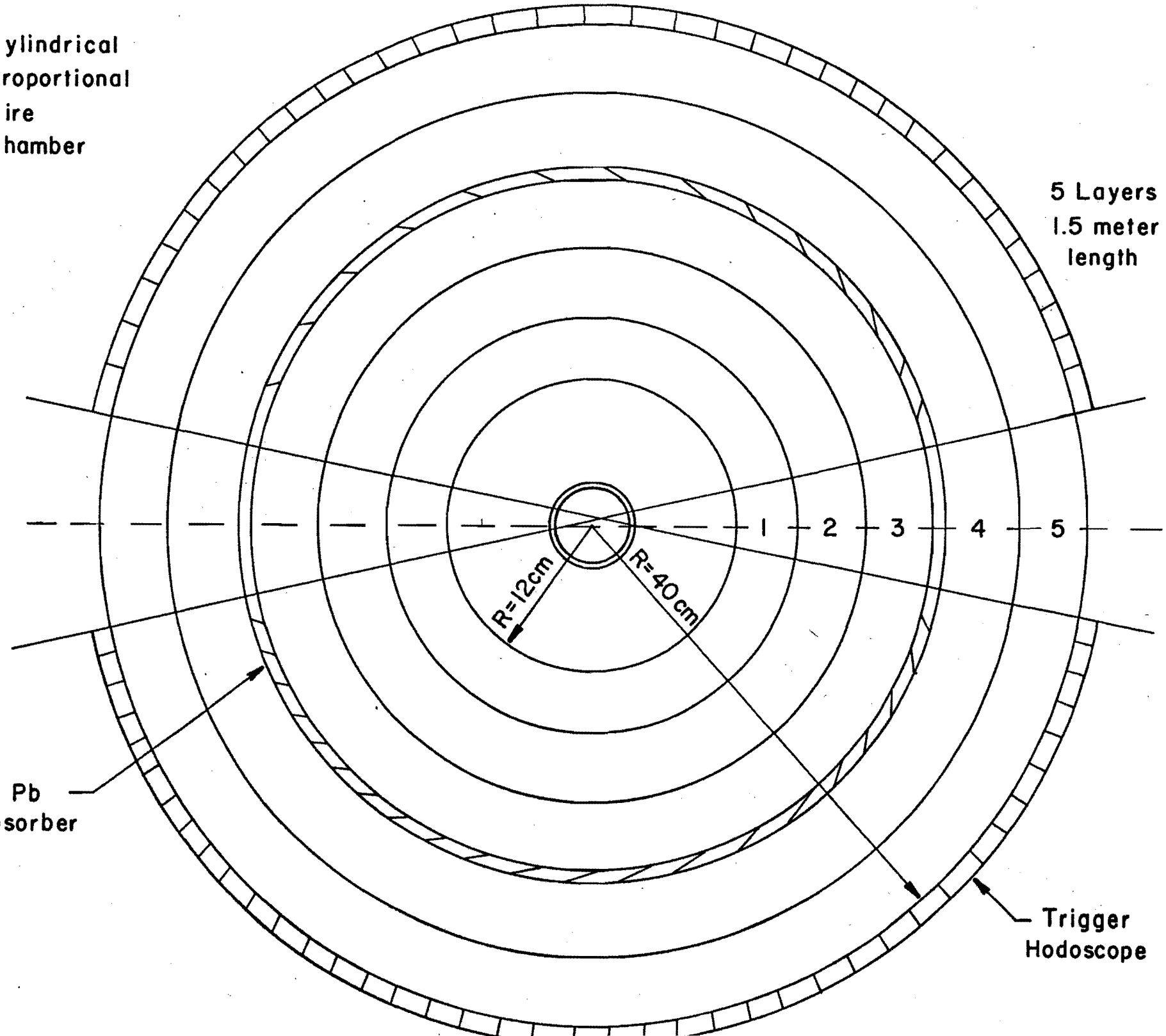

Fig. 10. Cross section of the cylindrical proportional chamber.

particle direction θ_2. Time of flight of the particle is measured by the large 1.0 meter × 6 meter hodoscope located about 2 meters from the intersecting region. For a 2 meter flight path it will be possible to identify charged electrons, pions, kaons, and protons over a momentum range of $0.1 \leq p_t \leq 1.0$ GeV/c. We have designed a threshold Cerenkov counter that can separate the electrons from muons and hadrons. The threshold Cerenkov counter (see Appendix IV) is segmented so that ambiguities due to several particles traveling through the spectrometer are eliminated.

Table I

Specifications of the magnetic spectrometer.

Quantity	Symbol	resolution (nominal)
momentum resolution at 1 $\frac{GeV}{c}$	$\frac{\Delta p}{p}$	3%
time resolution	Δt	$\sim$ 400 ps
flight path	ℓ	2 meters
probability of observing one particle of $\langle n_c \rangle$ for $\lvert y \rvert \leq 1.3$	$\frac{\Delta\phi}{2\pi} \frac{dn}{dy} \cdot y$	$\frac{1}{4} \frac{dn}{dy}$
pion proton time difference at P_t = 1.0 GeV/c	Δt	2.1 ns

The expected performance of this spectrometer is in line with the published results of the Argo low momentum spectrometer[20] and the CERN UA2 particle spectrometers.[21] The magnet has been designed so that adequate homogeneity of the $\vec{B}$ field is obtained and that uncertainties in the fringe field does not interfere with the event reconstruction and the operation of the accelerator. The detailed structure of the drift chambers and hodoscopes of this low momentum spectrometer are presented in Appendix IV.

B. "End Caps"

The "end cap" multiplicity counters are 6 layers of drift chambers. The inner three chambers count the charged particle multiplicity n_c. We can translate the pseudorapidity range $|y| \geq 9.2$ for Centauro events to the center of mass at $\sqrt{s}$ = 2 TeV and find the kinematical range is about $|y| \geq 2$. The pseudorapidity range $2 < |y| < 3.5$ is covered by a rectangular array whose area is about one square meter. Using the observed rapidity distribution at the CERN collider at $\sqrt{s}$ = 0.54 TeV,[21,22] we estimate that of the $n_c = 75$ expected for $|y| \geq 2$ we would observe 25 charged particles in both end caps. The neutrals are converted by an absorber after the third layer and counted by the outer three layers. Since for a multipion event $n_\gamma \sim n_c$ a clear signature would result for $n_\gamma \sim 0$. The details of these chambers are in Appendix V.

C. Trigger Hodoscope

A single layer scintillation hodoscope surrounds the CPWC and the outer layer of the end caps. A fast nanosecond trigger for a multiparticle event $n_c \geq n_{max}$ selects out events whose transverse momentum is $\sim 0.6\, n_c$ Gev/c.where n_{max} denotes the value at which the multiplicity distribution peaks in Fig. 5. For $n_c = 35$ this would correspond to a transverse momentum of $\sim$ 20 GeV/c or about 20% of the highest transverse momentum event of 100 Gev/c which we could study.

A second function of the end cap trigger hodoscope is to select out those charged and neutral particle tracks in the drift chamber which are in fast coincidence with the trigger hodoscope around the CPWC. This will serve to reduce background tracks by a factor

$$\frac{t_{drift}}{t_{coincidence}} = \frac{300}{15} = 20 \ .$$

IV. Counting Rates

The charged particle multiplicity distribution observed at the CERN collider ($\sqrt{s}$ = 0.54 TeV) by the UA5 apparatus[22] is shown in Fig. 5. At $\sqrt{s}$ = 2 TeV we expect a total cross section of above 65 mb. The inelastic cross section is expected to be 50 mb. If we assume that the distribution of charged particles does not change radically for $\sqrt{s}$ = 2 TeV then the number of events that are five times the most probable multiplicity is about 10^{-4} n_{max}. Since n_{max} should scale according to $a_0 + a_1 \ln s + a_2(\ln s)^2$, at $\sqrt{s}$ = 2 TeV we expect n_{max} = 35; about 67% of these will be within the coverage of our detector. To obtain a good value for $\langle P_t \rangle$ for a given bin of n_c, we want $\sim$2000 events in the dN/dP_t distribution; hence for 2000 events at $n_c = 5n_{max}$, we would have 3×10^8 total events for a minimum bias trigger. If we assume that we are exposed to a luminosity of $L = 10^{27}cm^{-2}sec^{-1}$ at DO for 10^7 secs, the total number of events N is; $N = 10^{27}cm^{-2}sec^{-1} \times 50\ 10^{-27}cm^{-2}sec^{-1} \times 10^7sec = 5 \times 10^8$ events. Hence a run of 10^7 sec is quite adequate; clearly we must heavily scale down the number of events accepted at low multiplicity in order to limit the total data sample to a manageable number, e.g. 2×10^6 events.

We can simply estimate the double interaction problem. The probability of a single interaction is a collision pulse for $L = 10^{27}cm^{-2}sec^{-1}$ is

$$\frac{50/sec}{140{,}000/sec} = 3.6 \times 10^{-4} .$$

The probability of a real event with multiplicity 2 n_{max} is 3.6×10^{-5}. We would expect an accidental double vertex background rate of $(3.6 \times 10^{-4})^2$ or 3% of the real rate. For $L = 10^{28}cm^{-2}sec^{-1}$, this would rise to 30%. However tracking through the cylindrical chambers would further reduce this by a factor of 50, i.e., 0.6% of the real rate.

V. Cost Estimate

An itemized cost estimate is given in Appendix VII; it sums up to 1.5 M$.

References

1. E. Fermi, Prog. Theor. Phys. 5, 570 (1950).

2. L. D. Landau, Izv. Akad. Nouk. S.S.S.R. 17, 51 (1953).

3. M. Gell-Mann, Synchrotron Laboratory Report CTSL-20 (1961); M. Gell-Mann, Phys. Lett. 8, 214 (1964); C. Zweig, CERN Report Nos. TH 401, 402 (1964).

4. J. D. Bjorken, Phys. Rev. 179, 1547 (1969); J. D. Bjorken and E. A. Paschos, Phys. Rev. 185, 1975 (1969); S. J. Drell, D. J. Levy and T. M. Yan, Phys. Rev. Lett. 22, 744 (1969).

5. D. Gross and F. Wilczek, Phys. Rev. Lett. 30, 1343 (1973); H. D. Politzer, Phys. Rev. Lett. 30, 1346 (1973).

6. H. Georgi and H. Politzer, Phys. Rev. D 14, 1829 (1976).

7. L. D. McLerran and B. Svetitsky, Phys. Lett. 98B, 199 (1981); J. Kuti, J. Polonyi and K. Szlachanyi, Phys. Lett. 98B, 199 (1981).

8. L. Van Hove, Phys. Lett. 118B, 138 (1982); J. D. Bjorken, Fermilab Pub. 82/44-THY.

9. UA1 Collaboration, Phys. Lett. 118B, 167 (1982).

10. J. Engels et al., Nucl. Phys. B205, 545 (1982).

11. J. Kogut et al., University of Illinois (Urbana) preprint ILL-(TH)-82-39, November (1982).

12. J. G. Rushbrook, Proc. of the 21st Int. Conf. on High Energy Physics CS-111.

13. A. T. Laasanen et al., Phys. Rev. Lett. 38, 1 (1977).

14. J. Erwin et al., Phys. Rev. Lett. 1534, 27 (1971).

15. D. Brick et al., Nucl. Phys. B152, 45 (1979).

16. T. F. Hoang, Phys. Rev. D 8, 2315 (1973).

17. C. M. G. Lattes, Y. Fujimoko and S. Hasegawa, Phys. Rep. 65, 152 (1980).

18. G. Domokos and J. L. Goldman, Phys. Rev. D 23, 203 (1981); G. Domokos, JHU-HET 8212 (1982); G. Domokos, JHU-HET 8301 (1983).

19. UA1 Collaboration, Phys. Lett. 122B, 189 (1983).

20. E. W. Anderson et al., Nucl. Inst. and Meth. 122, 587 (1974).

21. J. P. Rapellin, CERN UA2 Collaboration, Proc. of the 21st Int. Conf. on High Energy Physics C3-571; M. Banner et al., Phys. Lett. 122B, 322 (1983).

22. P. Carlson, CERN UA5 Collaboration, Proc. of the 21st Int. Conf. on High Energy Physics C3-593.

Appendix I
Estimates of the Energy Density

We can estimate the energy density in the central region using a one dimensional model.[1] Consider a section of outgoing matter

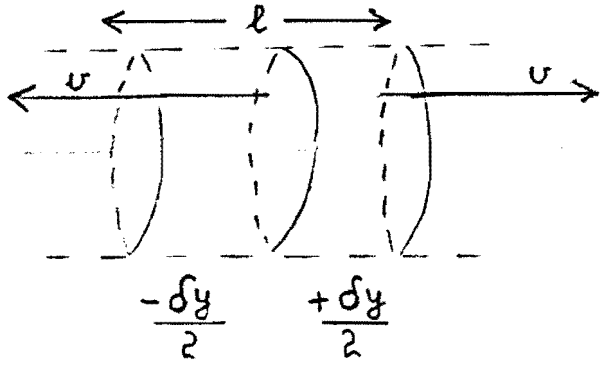

The volume of the cylinder $A \times \ell$ where

$$\ell \simeq 2vt \simeq t\delta y$$

where in the non-relativistic approximation

$$2v = \delta y$$

Let be the energy density and $A = \pi r^2$

$$\epsilon = \frac{1}{A \times \ell} \frac{dE_A}{dy} \delta y \qquad \epsilon = \frac{1}{t\pi r^2} \frac{dE_A}{dy}$$

t may be thought of as the lifetime of the thermalized blob. We can use experimentally determined values for pp collisions at $\sqrt{s}$ = 7.7 GeV.[2] Here t = 2fm and r_{11} = 0.7 fm. We assume $r_{11} \geq r_{\perp}$

$$t = 2 \text{ fm} \qquad r_{11} = 0.7 \text{ fm}$$

For pions

$$\frac{dE_A}{dy} \sim (0.4 \times \frac{3}{2}) \frac{dn_c}{dn}$$

where the 3/2 factor includes the contributions from π° mesons. Finally for

$$\frac{dn_c}{dy} = 8$$

$$\varepsilon = \frac{0.6}{2 \times \pi\ (0.7)^2} \qquad 8 \sim \frac{1.6\ \text{GeV}}{\text{fm}^3}$$

Studying high transverse energy events Bjorken argues[3] that energy densities substantially greater than our estimates may have been already observed at the CERN $\bar{p}p$ collider.

References to Appendix I

1. J. D. Bjorken, Fermilab Pub.-82/44 THY.
2. C. Ezell et al., Phys. Rev. Letters 38, 873 (1977).
3. J. D. Bjorken, Fermilab Pub.-82/59 THY.

Appendix II

The Sizes, Wire Spacings and Wire Counts of Wire Chambers

1. The end cap drift chambers (xuv)*

Width (cm)	Wire spacing (cm)	Number of wires	Double hit capability
50	1	50	yes
55	1	55	yes
60	1	60	yes
80	2	40	yes
90	2	45	yes
95	2	47	yes

Total number of wires = $3 \times 4 \times 300 = 3600$

N^{E}_{total} = 3600 wires length = 2 meters

2. The transverse drift chambers (xuv)*

Width (cm)	Wire spacing (cm)	Number of wires	Double hit capability
230	2	115	no
275	2	137	no
320	2	160	no

Total number of wires = 3 2 412 = 2472

N^{T}_{total} = 2472 wires length = 1 meter

3. The central cylindrical proportional chambers

Circumference (cm)	Wire spacing (cm)	Number of wires	Charge division
70	0.15	466	yes
105	0.20	525	yes
140	0.20	700	yes
175	0.20	870	yes
250	0.10	1250	yes

N^{C}_{total} = 3811 wires length = 1.5 meters

*u,v are rotated by ±16° with respect to x.

To determine the location of the hit along the wire of CPWC we will use charge division. To improve the conventional resolution we will investigate the possibility of operating our chambers in a self-quenching streamer mode.[1] This may improve the resolution by a factor of 10.

References to Appendix II

1. M. Atac, A. V. Tollestrup and D. Potter, Nucl. Inst. and Meth. 200, 345 (1982).

Appendix III

The Dimensions and Counts of Trigger Hodoscopes

1. The end cap trigger hodoscopes vertical

	Hodoscope width (cm)	Cross section (cm^2)	Number of segments	Light division
Vertical	100	2 × 1	50	yes
Horizontal	200	4 × 1	50	no

Total number hodoscope elements = 4 × 100 = 400

Vertical element length = 2 meters

Horizontal element length = 1 meter

2. The time of flight hodoscope

	Hodoscope width (cm)	Cross section (cm^2)	Number of segments	Light division
Vertical	530	5 × 2	106	yes

Total number of hodoscope elements = 2 × 106 = 212

Vertical element length = 1 meter

3. The trigger hodoscope on the cylindrical chamber

	Hodoscope radius (cm)	Cross section (cm^2)	Number of segments	Light division
Horizontal barrel	43	4 × 1	68	no

Total number of hodoscope elements = 68 × 2 = 136

Horizontal element length = 1.6 meters

Appendix IV
Parameters of the Spectrometer Magnet

The spectrometer magnet, whose vertical cross section (perpendicular to the beam) is shown in Fig. 11, consists of a pair of dipoles centered at 20" on either side of the beam. The four coils are connected in series such that the fields in the two 10" gaps are anti-parallel; this configuration allows the two magnets to share a common flux return path. The symmetry around the Tevatron beam ensures zero magnetic field there; field gradients, such as quadrupole and octopole, will exist but are expected to be manageable. The Main Ring beam is 3" above the top of the magnet yoke, allowing adequate space for magnetic shielding of the small fields that will exist there.

The mechanical parameters of the magnet are:

Yoke outer dimension, x:y:z = 45" × 45" × 76"
Gap height = 10", pole width = 5"
Coil cross section, x:y = 2 1/4" × 6 1/2"
Weight of iron = 5.6 t
Weight of 4 coils = 1.4 t
Angular acceptance: $\Delta\phi$ = 25°
$\Delta\theta$ = ±59° (n = ±1.3)

The magnet is designed to give a transverse deflection of 40 MeV/c to a particle traveling at θ = 90°. The magnetic and electrical parameters corresponding to this are:

Field at gap center = 3.5 kG
Coil current density = 3 ka/in
Power dissipation = 50 kw
Magnetic field in yoke = 7 kG

If the coils were wound with water cooled copper bus similar to that used in Main Ring dipoles (0.9 in^2 of copper), each coil would have 12 turns, yielding a magnet voltage of 17V. We estimate the total cost of the magnet to be 45K$.

MAGNET VERTICAL SECTION

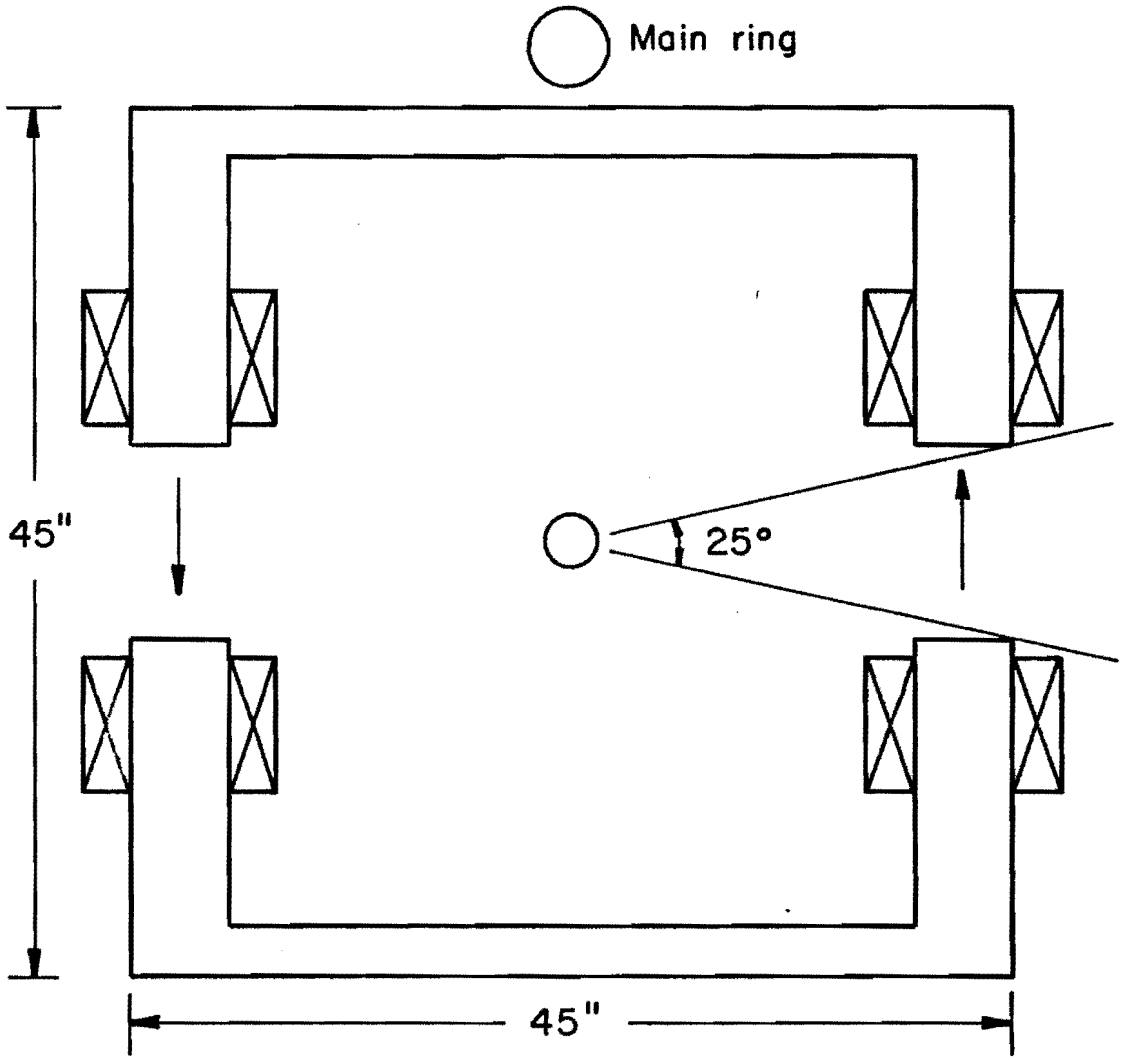

Fig 10

MAGNET TOP VIEW

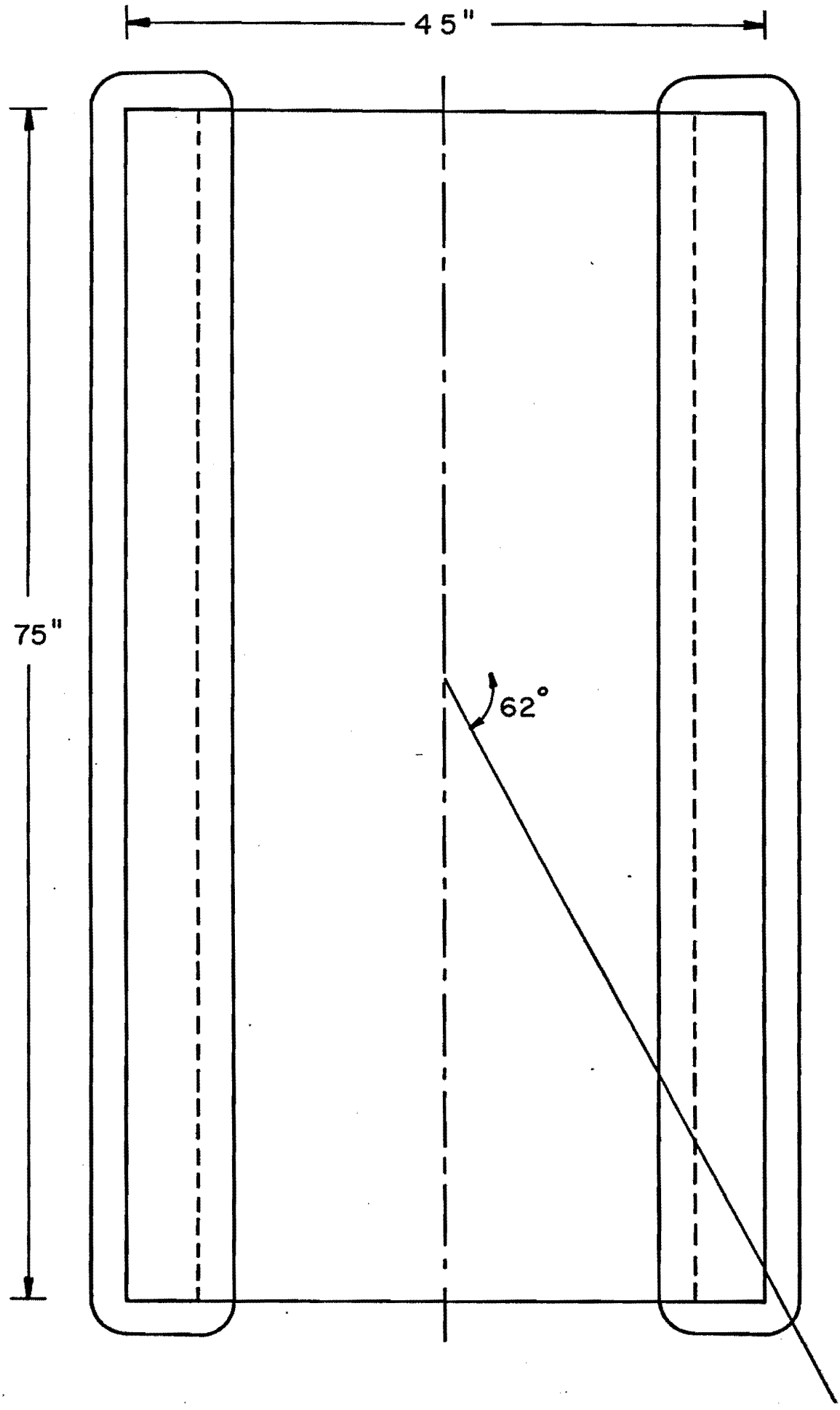

Appendix V
Description of the Cherenkov Counter

The threshold Cerenkov counters are atmospheric pressure room-temperature Freon-12 filled vessels. As the index of refraction is of Freon is 1.0011, only electrons are above threshold in the momentum range 10 MeV/c to 3 GeV/c. The Cerenkov counters are 1.5 meters deep, so that the expected number of usable photons is 130. These photons are highly collimated. The back dimensions of the counter are 2m by 9m and can be covered by 18 spherical mirrors (with clipped edges). These mirrors will be arranged so as to throw the light back to 18 phototubes (5 inch) arranged along the top and bottom of the front Cerenkov wall. We will use 5" RCA quantacon low noise phototubes (PT) or their equivalents. An example of mirror arrangement is shown below.

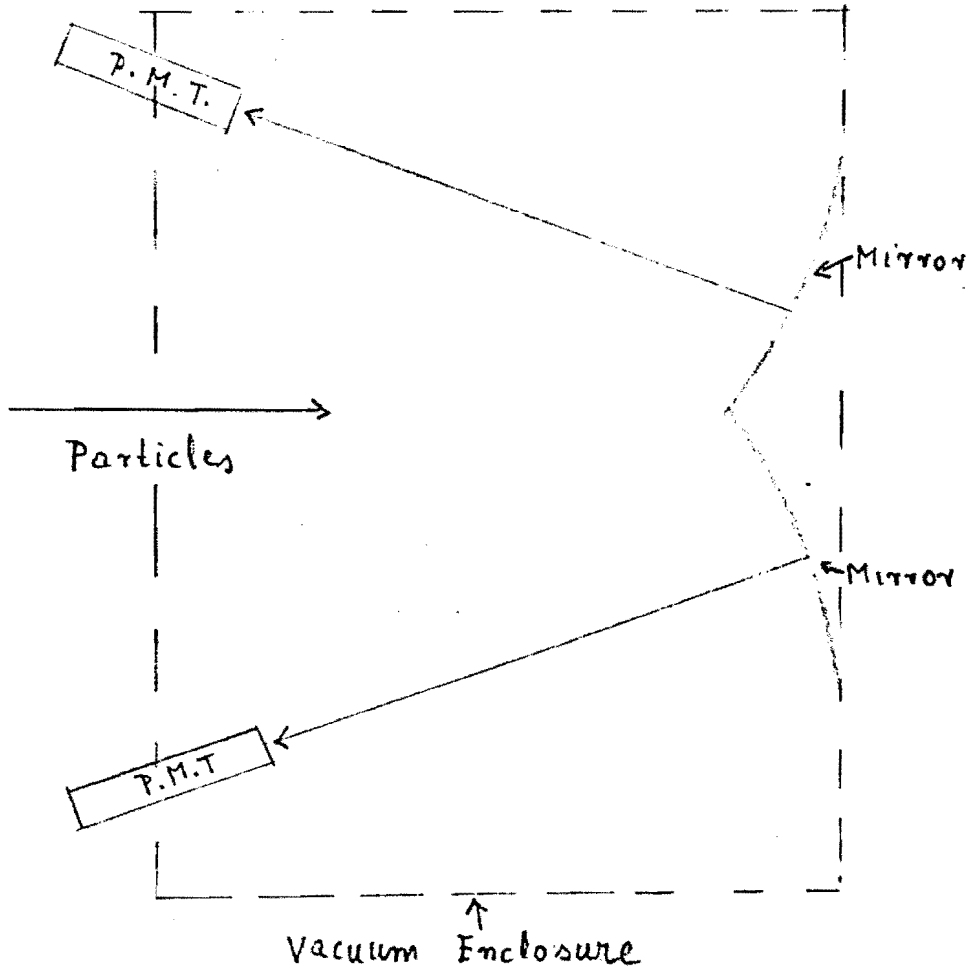

Appendix VI
Background Considerations

A. CPWC and End Cap Wire Chambers

Our experience in E591 with semiconductor detectors operating $\sim$ 30 cm from the main ring beam pipe indicates a flux of $\sim 10^4/cm^2sec$ minimum ionizing particles during the acceleration cycle of 10^{13} protons when the gas jet was not in operation. This means that a single drift chamber cell of area 200 cm^2 would sustain about one hit during the $\sim$ 0.5 μs drift time. Consequently, double hit capability is required on the end cap drift chambers. In addition the following precautions were taken: (a) One vertical scintillator rod backs up each cell of the last drift chamber. (b) Each vertical rod is equiped with photomultiplier tubes on each end to ensure light division capability. The above features make it possible to recognize the time correlated hit in the drift chamber cell, as by the time zero pulse from the central hodoscope. Thus background hits can be reduced by a factor of 500 n·s/10 n·s = 50.

We expect that this is a worse case argument, namely only $5 \cdot 10^{11}$ particles are circulating in the collider ring, the vacuum is much better and the beam is coasting. It is our understanding that the CERN SPS experience indicates that the background is indeed less than the estimates we have made based on the C_0 experience.

B. Lepton Pair Background

To reduce the lepton background we have to minimize the mass of the beam pipe and the walls of the CPWC so that only a minimum number of gamma rays are converted. If the beam pipe is constructed of 25 mil Be and the walls of the CPWC are aluminized mylar then it is reasonable to say that gamma rays see less than 10^{-2} of a radiation length. Further rejection of these events is provided by reconstruction of the pair events in the CPWC. An additional drift chamber in the magnetic field can be used to observe low $\leq$ 40 Mev/c momentum leptons. A background event would occur. When only one lepton from a pair is seen in each spectrometer, they are of opposite sign and have a low 200 - 600 Mev/c invariant mass. Thus it is

essential to be able to observe both leptons of pair in a high percentage of the events.

An additional source of background events are produced by energetic particles which strike the magnet yoke etc. We would use event reconstruction to eliminate these events the more accurately we are able to determine the interaction vertex the better the rejection factor. The use of the self-quenching streamer mode of operating the CPWC charge division would improve vertex resolution by a substantial factor.

C. Jet Events

Order of magnitude estimates[1] of the cross section for the production of a particle jet are $\sigma \sim 10^{-30}$cm when the transverse momentum P_t of the jet is 10 Gev/c. Since we are interested in events where $\sigma \sim 5 \cdot 10^{-26}$ for $n_c \sim 35$ to $\sim 5 \cdot 10^{-30}$ for $n_c = 175$. We must depend on event reconstruction to reject jet events. Such a jet would have several particles with a small $\leq 20°$ opening angle. We should be able to distinguish this type of event from a high multiplicity central event. Higher P_t jets have much lower cross sections.

Reference for Appendix VI

1. Design report for the Fermilab collider CDF, August 1981, page 40.

Appendix VII
Cost Estimates

		In Thousands
1.	End cap drift chamber electronics, LeCroy T.D.C. 3600 wires with double hit capability	324.0
2.	Transverse drift chamber electronics, LeCroy T.D.C. 2472 wires	123.6
3.	Central cylindrical proportional chamber electronics with charge division, LeCroy 0.1 pico coulomb / channel A.D.C. 3811 wires, 2 channels ea required	404.0
4.	Trigger hodoscope for end cap 400 element, 200 required with light division	60.0
5.	Trigger hodoscope for central chamber 126 elements	12.6
6.	Time of flight hodoscope, 212 elements with light division	424.0
7.	Cherenkov Counter, 36 light collection segments, R.C.A. 8854 quanticon	72.0
8.	Magnet iron and coils	45.0
	Total	1465.2 K

rec'd 9/21

P-735, Revised

Sept. 16, 1983

SEARCH FOR A DECONFINED QUARK GLUON PHASE OF STRONGLY INTERACTING MATTER IN $\bar{p}$-p INTERACTIONS AT $\sqrt{s} \approx 2$ TeV

Submitted by Scientists at Duke University,
the Fermi National Accelerator Laboratory,
Purdue University, and the University of Wisconsin

Abstract

We propose to use a magnetic spectrometer and a central tracking chamber located at the CO intersection area that can utilize low luminosity, from 10^{27} to 10^{29} cm^{-2} sec^{-1}, to measure the transverse momentum distributions dN/dp_t up to p_t = 1.4 GeV/c for centrally produced $p^{\pm}$, $K^{\pm}$, $\pi^{\pm}$ and γ as a function of the charged particle multiplicity n_c. The temperature T and the size of centrally produced plasma can be extracted from the transverse momentum (p_t) distributions dN/dp_t and from the like pion correlations, respectively.

Evidence for a quark gluon plasma manifests itself by

(a) Breaks in $\langle p_t \rangle$ as a function of dn_c/dy in the central region $|y| \leq 1$.

(b) Changes in the particle composition as a function of the charged particle multiplicity n_c.

(c) Onset of low energy ($E_\gamma \approx 200$ MeV) direct photon production with increasing charged particle multiplicity n_c.

Because we momentum analyze only low energy particles in observing these signatures, the size and cost of this apparatus is one tenth of that required for a 4π detector which studies high transverse momentum reactions.

Person to contact: L. J. Gutay
Commercial phone: (317) 494-5047
FTS phone: 284-5390

Names of the Senior $\bar{E}$xperimenters

Duke University:

A. T. Goshaw
L. R. Fortney
P. W. Lucas
W. J. Robertson
W. D. Walker

Fermilab:

F. Turkot

Purdue University:

A. Bujak
D. D. Carmony
Z. W. Grabowski
L. J. Gutay
A. S. Hirsch
N. T. Porile
F. A. Rickey
R. P. Scharenberg
P. C. Simms
B. C. Stringfellow

University of Wisconsin:

A. Erwin
M. Thompson

I. Introduction

Although the original models for particle production were statistical and thermodynamic in nature (Fermi[1] and Landau[2]), the main thrust of high energy physics has been the study of particles and resonances. The fact that these have definite quantum numbers and could be classified into various representations of symmetry groups by Gell-Mann[3] as well as the existence of Bjorken scaling[4] has led to the hypothesis that hadrons are made of quarks and gluons.

The absence of any evidence for the existence of free quarks has led to the concept of quark confinement. From the concept of asymptotic freedom[5] QCD evolved[6] as the theory of strong interactions in agreement with numerous hard scattering experiments. Both thermodynamical bootstrap and lattice gauge calculations of QCD predict a phase transition from hadrons to a quark-gluon plasma at sufficiently high temperatures and/or quark densities.[7] There is a general theoretical concensus that temperatures of $T \sim 200$ MeV and/or quark antiquark densities of $n_q + \bar{n}_q = 2$ to 4 per cubic fermi are required to produce a quark-gluon plasma.[8] Such a density may be thought of as two protons being "placed on top of each other."

The energy density vs T for a phase transition[9] from SU_3 lattice gauge calculations is shown in Fig. 1 for a gluon plasma. Similar results have been obtained from lattice gauge calculations using SU_2 Yang Mills theory.[10] To cast Fig. 1 into a form that can be related to experimental quantities, we multiply the ordinate axis of Fig. 1 by T^3. The general shape remains unchanged as shown in Fig. 2 where we introduced the symbol $\sigma = \frac{\varepsilon}{T}$, the entropy density. According to statistical mechanics and thermodynamics, the entropy density is proportional to the rate of particle production over unit rapidity interval ($\sigma \propto \frac{dn}{dy}$) and the temperature is proportional to the average transverse momentum

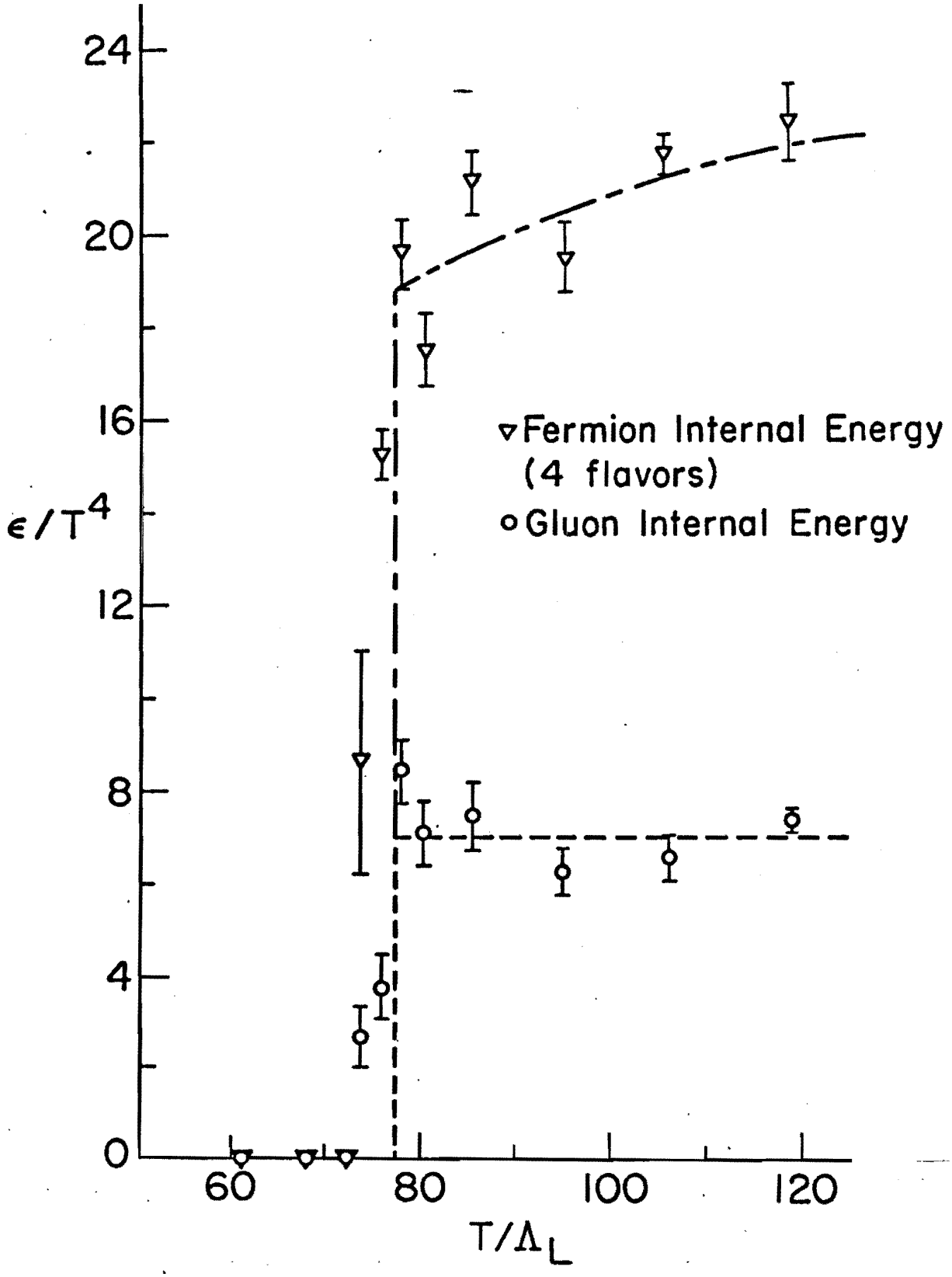
24
20
16
12
8
4
0
ϵ/T^4
60
80
100
120
T/Λ_L
▽Fermion Internal Energy
(4 flavors)
○Gluon Internal Energy

Fig. 1

($T \propto \langle p_t \rangle$). Thus from the above relations and Fig. 2 we can deduce the shape of dn/dy as a function of $\langle p_t \rangle$ as shown in Fig. 3. As discussed in the next section (II), it is possible to quantitatively calibrate $\langle p_t \rangle$ versus T so that the critical (deconfinement) temperature can be determined. The distribution dn_c/dp_t for pions must be a Bose-Einstein distribution in the range $p_t \leq 1.0$ GeV/c. It should then be possible to speak of a thermalized energy density.

One of the unexpected results of the CERN $\bar{p}$-p collider was the observation of high multiplicity, high transverse momentum, non-jet, isotropic events. Further, these events have a far larger cross section than jet events[11] (See Fig. 4). These data led Bjorken[8] to conclude that energy densities well above the expected phase transition energy densities may already exist at the CERN $\bar{p}$-p collider energies. This experiment also observed that the transverse energy in these events is proportional to the number of low transverse momentum particles (See Fig. 5). It is this basic correspondence that will be exploited in the experiment we propose. These results also lead naturally to a thermodynamical interpretation. In fact, evidence for thermalization at lower energies and multiplicities has been observed with T = 120 MeV. Our estimates suggest (See Section II) that at $\sqrt{s}$ = 2 TeV and $n_c > 50$ we will be able to attain temperatures $T \gtrsim 200$ MeV and energy densities ~ 2.0 GeV per cubic fermi (See Appendix I).

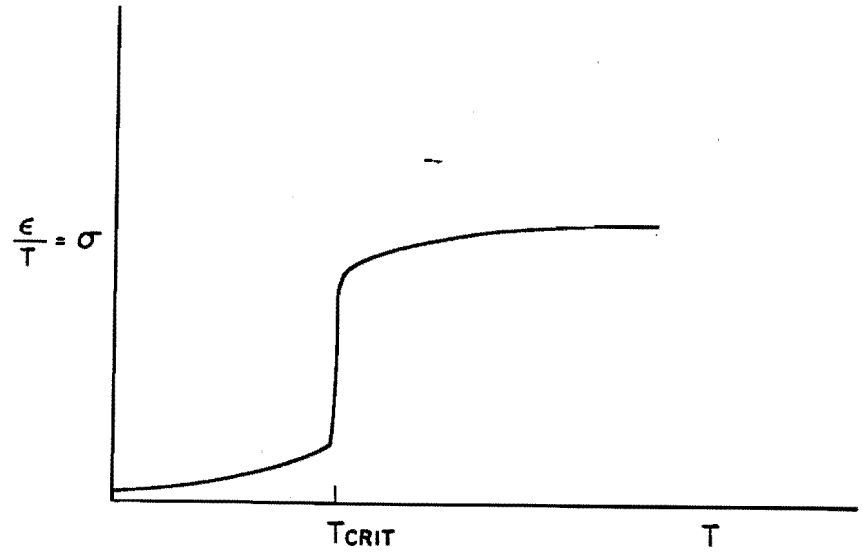
$\frac{\epsilon}{T} = \sigma$
T_{CRIT}
T

Fig. 2

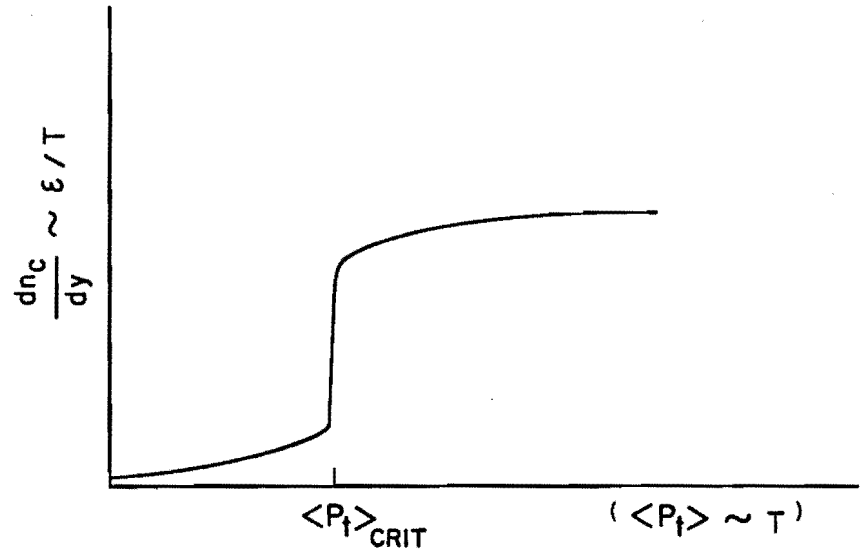
$\frac{dn_c}{dy} \sim \epsilon / T$
$\langle P_t \rangle_{CRIT}$
($\langle P_t \rangle \sim T$)

Fig. 3

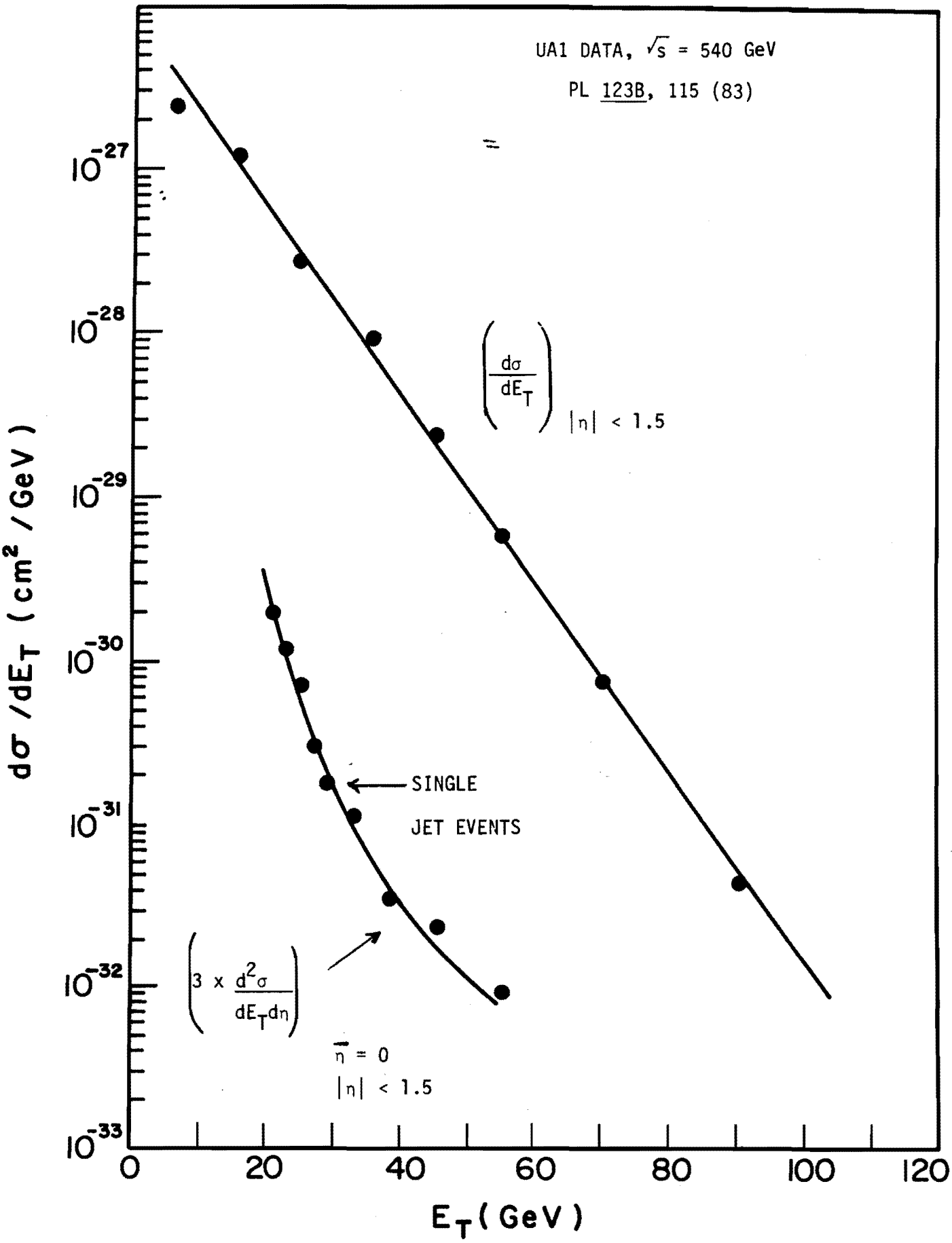
UA1 DATA, $\sqrt{s}$ = 540 GeV
PL 123B, 115 (83)
$\left(\frac{d\sigma}{dE_T}\right)$ $|\eta| < 1.5$
SINGLE
JET EVENTS
$\left(3 \times \frac{d^2\sigma}{dE_T d\eta}\right)$
$\bar{\eta} = 0$
$|\eta| < 1.5$
$d\sigma/dE_T$ (cm^2 / GeV)
E_T (GeV)
10^{-27}
10^{-28}
10^{-29}
10^{-30}
10^{-31}
10^{-32}
10^{-33}
0
20
40
60
80
100
120

Fig. 4

$\bar{P}P$, UA1, $\sqrt{s}$ = 540 GeV

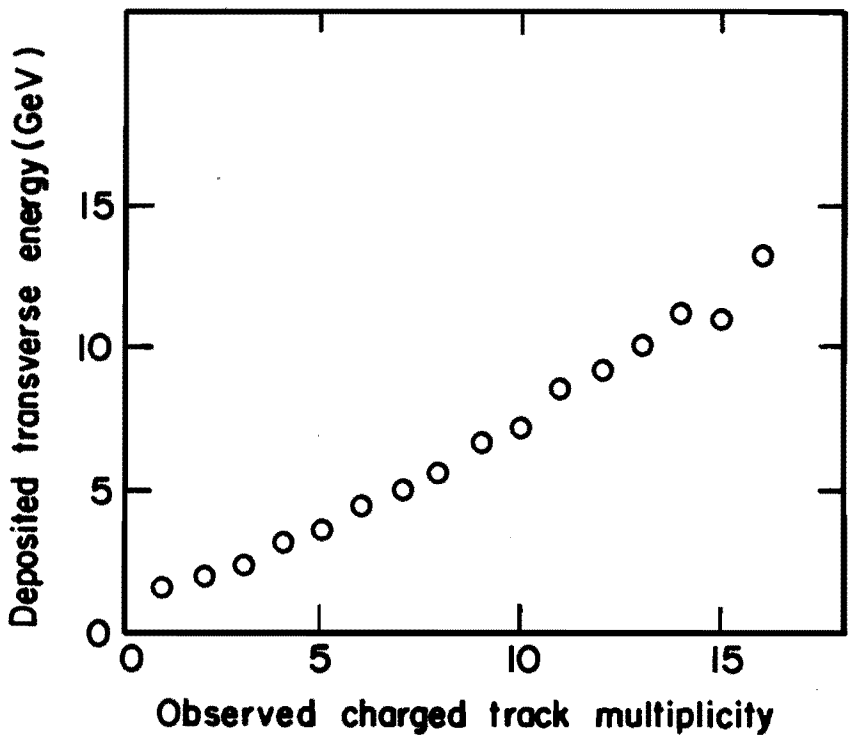

Deposited transverse energy as a function of observed charged particle multiplicity.

[Phys. Lett. 107B, 320 (1981)]

Fig. 5

II. Physics Scope of the Experiment

A. Hadrons Emerging from the Quark-Gluon Plasma

To study the central region of $\bar{p}p$ collisions in the CO area of the Fermi National Accelerator Laboratory at a center of mass energy of 2 TeV, we propose using a low momentum magnetic spectrometer with particle identification. We will measure the transverse momentum (p_t) distribution of centrally produced $p^{\pm}$, $K^{\pm}$, $\pi^{\pm}$, and γ for $p_t < 1.4$ GeV/c as a function of the charged multiplicity $N_D \equiv \int_{-3}^{3} (dn_c/dy)dy$ ($\sim 2/3$ of the total).

It has been observed[12] at the CERN $\bar{p}p$ collider ($\sqrt{s} = 0.54$ TeV) that the number of charged particles in the central region is larger than those observed at ISR energies, and that there exists a clear dependence of $\langle p_t \rangle$ in the central region on the central multiplicity n_c (Fig. 6).[13] It has been pointed out[8] that this increase in $\langle p_t \rangle$ as a function of n_c could result from the combined effects of transverse expansion and temperature caused by the energy which has been deposited in the central region.

The increase of $\langle p_t \rangle$ with dn/dy is the same at the CERN-collider, the ISR, and for fixed target Fermilab data for the common range of dn/dy. Figure 6 shows a cessation of the rise in $\langle p_t \rangle$ with increasing dn/dy which is compatible with a phase transition (See Fig. 3); that is, as the entropy density ($\varepsilon/T \propto dn/dy$) continues to increase the temperature ($T \propto \langle p_t \rangle$) remains constant. From data at a single $\sqrt{s}$ we cannot rule out that this is merely a kinematic effect. It is therefore important to repeat this measurement at $\sqrt{s} = 2$ TeV where the range of dn/dy is at least 1.5 times as great simply from the ln(s) effect. Since the CERN-collider experiments[14] have reported (Fig. 7) an excess of high multiplicity events as compared to a KNO scaling curve[15,16] (or in comparison

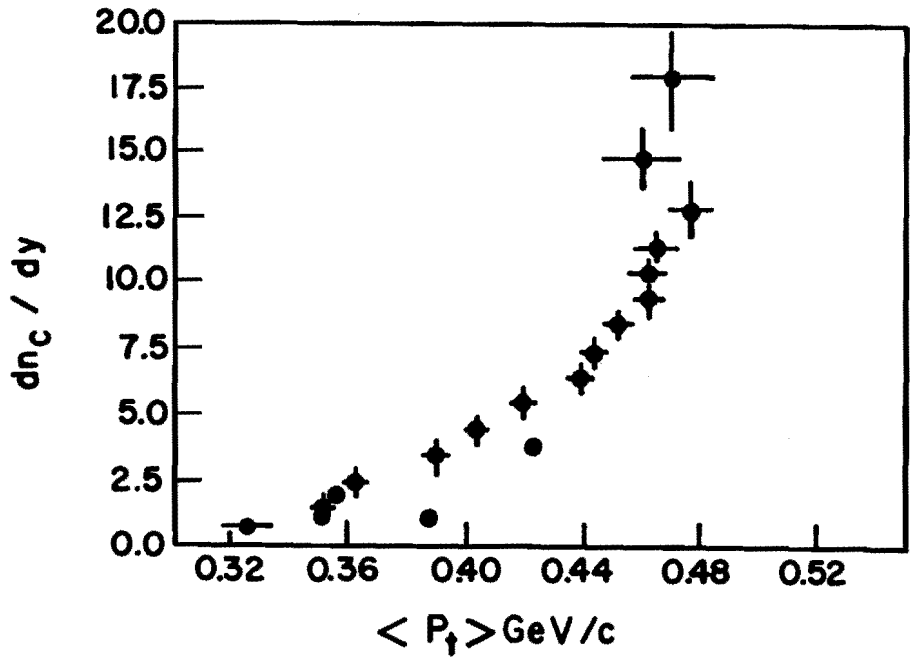

Fig. 6. The mean transverse momentum of charged hadrons ($\sqrt{s}$ = 540 GeV) as a function of charged track multiplicity in the rapidity interval $|y| < 2.5$. (Error bars are purely statistical.) From Ref. 13. To be compared with Fig. 3. Data from three other experiments are included, pp ISR (63 GeV), pp FNAL (19.6 GeV), pp FNAL (19.6 GeV).

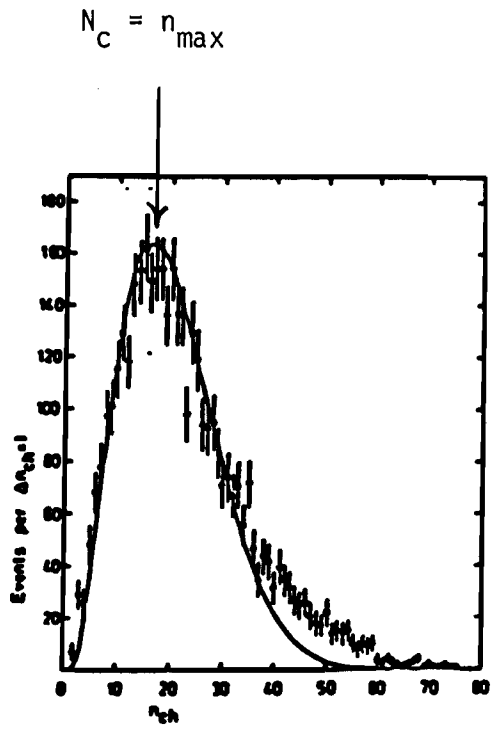

Fig. 7. The distribution of observed charged multiplicities in the UA5 experiment. Errors shown are statistical. The curve is a fit to lower energy data and scaled to $\sqrt{s}$ = 540 GeV. From Ref. 14.

to ISR) the assumed $n_c \sim \ln(s)$ underestimates the available dn/dy range at Fermilab.

Our group has studied pion production in the central region[17] in pp collisions at $\sqrt{s}$ = 7.7 GeV. The observed p_t distribution can be quantitatively interpreted in terms of a thermodynamic picture where the distribution dn/dp_t yields a Bose-Einstein statistical distribution from which a temperature of 117 MeV can be extracted. The fit to the data is shown in Fig. 8. Other authors have found similar values for the temperature of hadronic matter at SLAC,[18] FNAL,[19] and ISR[20] energies.

In our work,[17] the determination of T = 117 MeV involved 4, 6, 8, and 10 prong events. If we assume that $\bar{n}_c = 5$ for these events this corresponds to $\frac{d\bar{n}_c}{dy} \sim 1.3$. Accepting the thermodynamical relations, which are valid outside the region of phase transition;

$$\frac{dn}{dy} \propto T^3$$

we can estimate the critical value of dn/dy as follows:

$$\frac{\left(\frac{dn_c}{dy}\right)_{crit}}{1.3} = \left(\frac{T_{crit}}{117}\right)^3 = \left(\frac{215}{117}\right)^3 .$$

Using the theoretically predicted[10] T_{crit} of 215 MeV we obtain

$$\left(\frac{dn_c}{dy}\right)_{crit} = 8 .$$

The subscripts "c" and "crit" denote charged and critical, respectively. As a cross check, with $dn_c/dy = 8$ we estimate the energy density in the central region, ε, using a one dimensional model as given in Appendix I. To evaluate

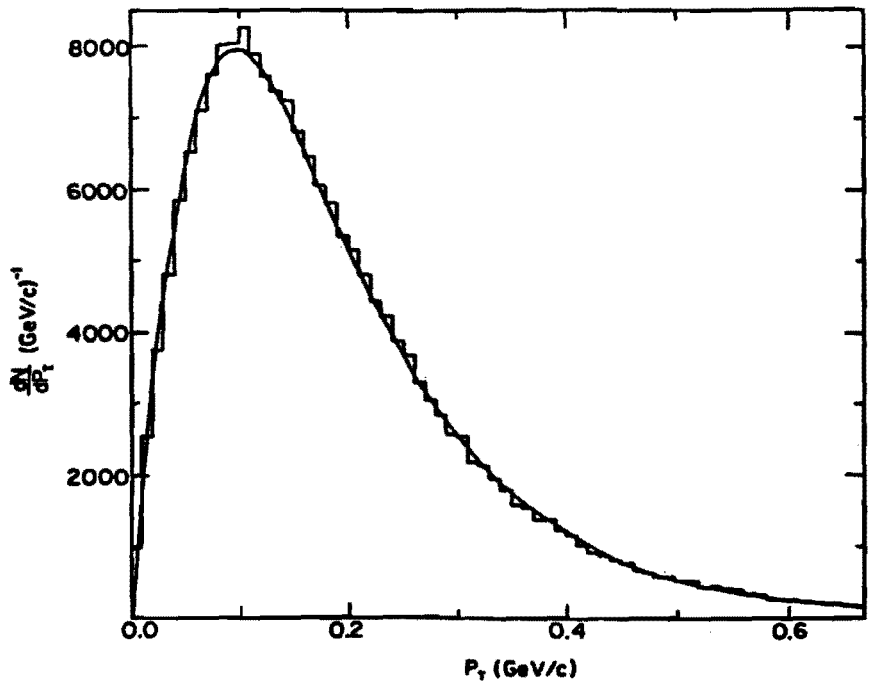

Fig. 8. The transverse-momentum distribution for central particles in the asymptotic large-multiplicity limit in the reaction $p_1 + p_2 \rightarrow p_3 + X$. The curve is a fit to the Bose-Einstein statistical distribution. From Ref. 17.

ε, one needs the typical size and lifetime of the centrally produced hadronic flux. This can be obtained by this experiment using the Hanbury-Brown and Twiss method applied to pions as discussed in Section D below.

As shown in Fig. 6, the mean transverse momenta $\langle p_t \rangle$, at $\sqrt{s}$ = 0.54 TeV has been measured as a function of dn_c/dy in the range 1 to 15 and indeed it is observed that $\langle p_t \rangle$ becomes a constant for $\frac{dn_c}{dy} > 8$. This indicates that temperatures on the order of twice those attainable at $\sqrt{s}$ = 7.7 GeV may just be reached at $\sqrt{s} \sim .5$ TeV. However, the experiment needs to be done at higher energies to rule out kinematic effects, i.e., lack of available energy, and with much higher statistics. The flattening of $\langle p_t \rangle$ has also been detected for very complex events by the Brazil-Japan cosmic ray collaboration.[21]

It should be pointed out that the UA1 measurement of $\langle p_t \rangle$ shown in Fig. 6 was made <u>without</u> particle identification. The p_t spectra <u>with</u> particle identification in the p_t range 0.5 - 1.05 GeV/c ($|\eta| < 0.6$) with minimum bias trigger (hence the data sample is dominated by events having $N_D = \langle N_D \rangle$) as measured by UA2[14] is shown in Fig. 9. From this graph one observes that: (a) $\langle p_t \rangle$ depends on particle type (the well-known fact that $\langle p_t \rangle$ increases with mass) and (b) the ratio $(K + p)/(\pi + K + p)$ changes from 18% at p_t = 0.5 GeV/c to 27% at p_t = 1.0 GeV/c. Since the suggestion of a plateau in the UA1 data of Fig. 6 is a subtle effect involving a 10 - 20% change in $\langle p_t \rangle$ <u>vs</u> dn/dy, it seems clear that a real exploration of this effect requires particle identification.

The distributions dN/dm_t will be studied for each of the particle types $\pi^{\pm}$, $K^{\pm}$, and $p^{\pm}$, to extract a value of the temperature T, i.e., $dN/dm_t(m_t) \propto e^{-m_t/T}$, ($m_t = \sqrt{m^2+p_t^2}$) as a function of the detected charge particle multiplicity N_D.

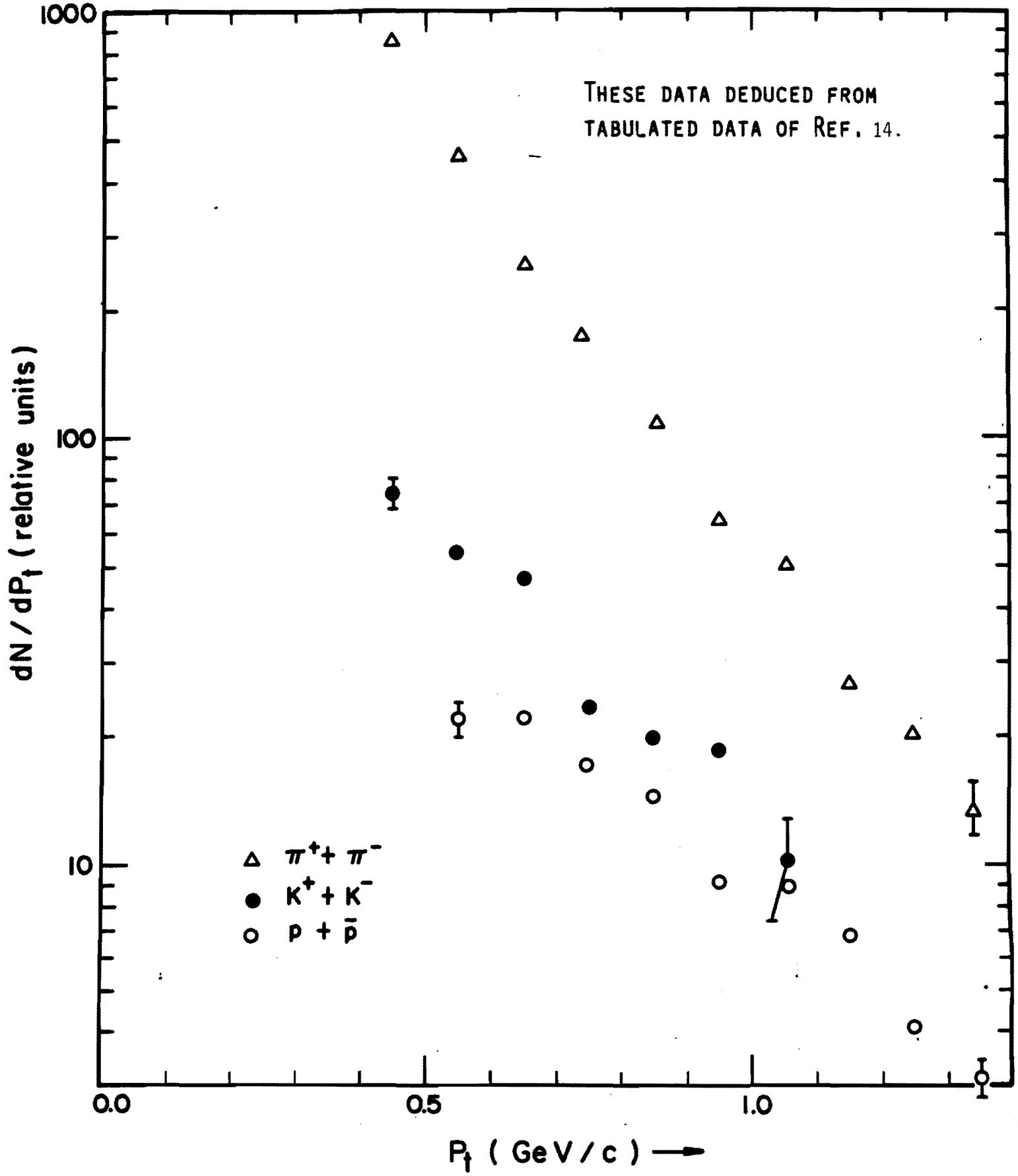
THESE DATA DEDUCED FROM
TABULATED DATA OF REF. 14.
1000
100
10
dN / dP_t (relative units)
π⁺ + π⁻
K⁺ + K⁻
p + p̄
0.0
0.5
1.0
P_t (GeV / c) ⟶

FIGURE 9

Finally, the K/π and p/π ratios are of interest in their own right and will be studied as a function of the detected charged particle multiplicity, N_D. Some enhancement of the K/π ratio is a likely consequence of the phase transition.

B. Photons Emerging from the Quark-Gluon Plasma

So far we have discussed how a quark-gluon plasma would manifest itself by emission of strongly interacting particles. As opposed to hadrons, particles which interact electromagnetically can emerge from the quark-gluon plasma anytime during the existence of the plasma. The accessible range of photon energy (E_γ) relevant to quark-gluon plasma formation is from 50 MeV to 1 GeV. Thus the study of the dn_c/dy dependence of both the cross section and energy (E_γ) distribution of photons emerging from $\bar{p}$-p collisions are of great importance. These photons come from two basic sources: 1) secondary products of decaying hadrons (N_γ^{had}), and 2) primary direct photon emission from processes such as quark-gluon Compton scattering, $q\bar{q}$ annihilation, and internal quark bremmstrahlung emission. Halzen and Liu[22] have predicted that the latter source of direct photons will become important when the plasma is formed. The increase of the γ cross section, due to the onset of direct photon production can be as large as 10% to 30% of the hadron cross section as sketched in Fig. 10a, where N_γ is the total photon yield and N_{had} the hadron yield. The non-direct photons (N_γ^{had}) arise from π^o and η^o decays. While the photon rate from π^o decay can be determined from the measured π^+ and π^- rates, the photon rates from η^o cannot be determined in this experiment. It is reasonable to assume that the cross section ratio σ_π/σ_η does not vary with dn/dy and thus the flat portion of N_γ/N_{had} (See Fig. 10b) below $(dN/dy)_{crit}$ defines N_γ^{had}/N_{had},

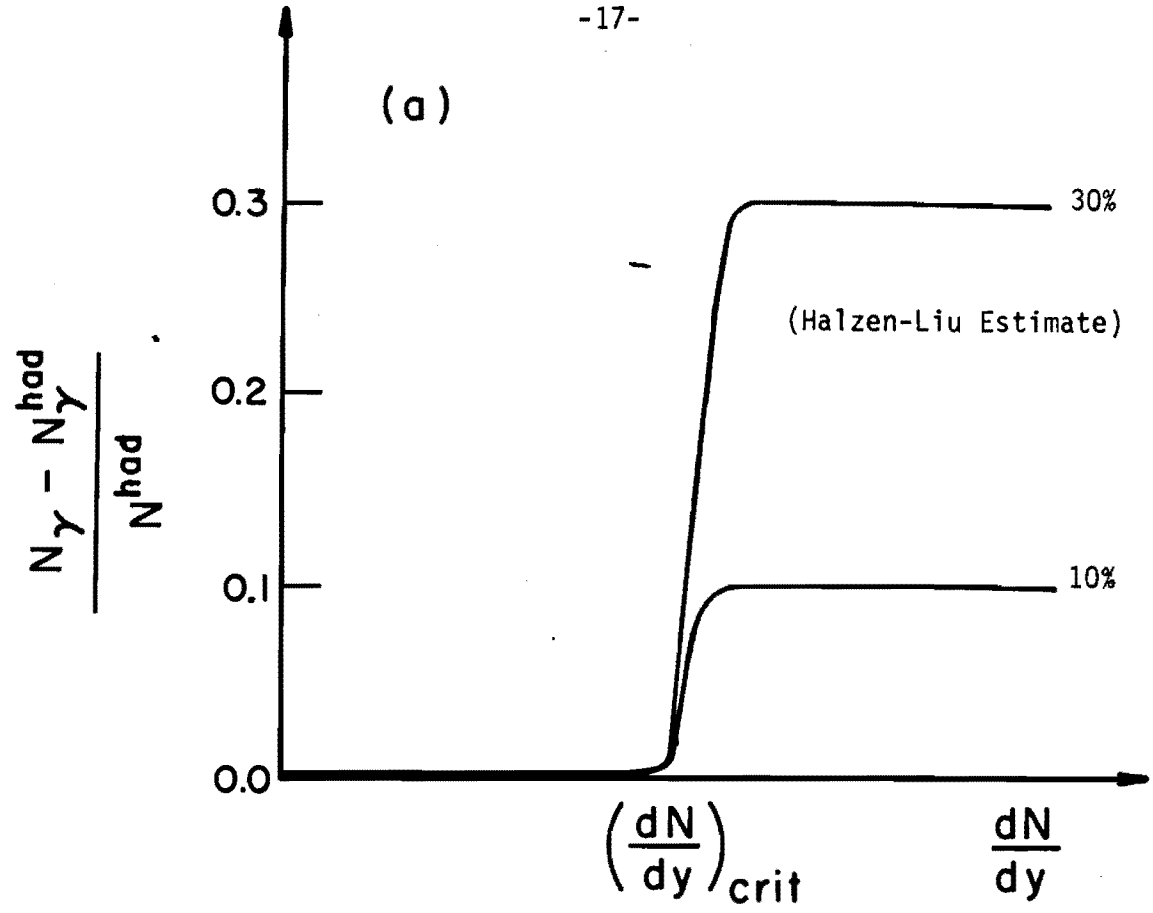
(a)
0.3
0.2
0.1
0.0
30%
(Halzen-Liu Estimate)
10%
$\frac{N_\gamma - N_\gamma^{had}}{N^{had}}$
$\left(\frac{dN}{dy}\right)_{crit}$
$\frac{dN}{dy}$

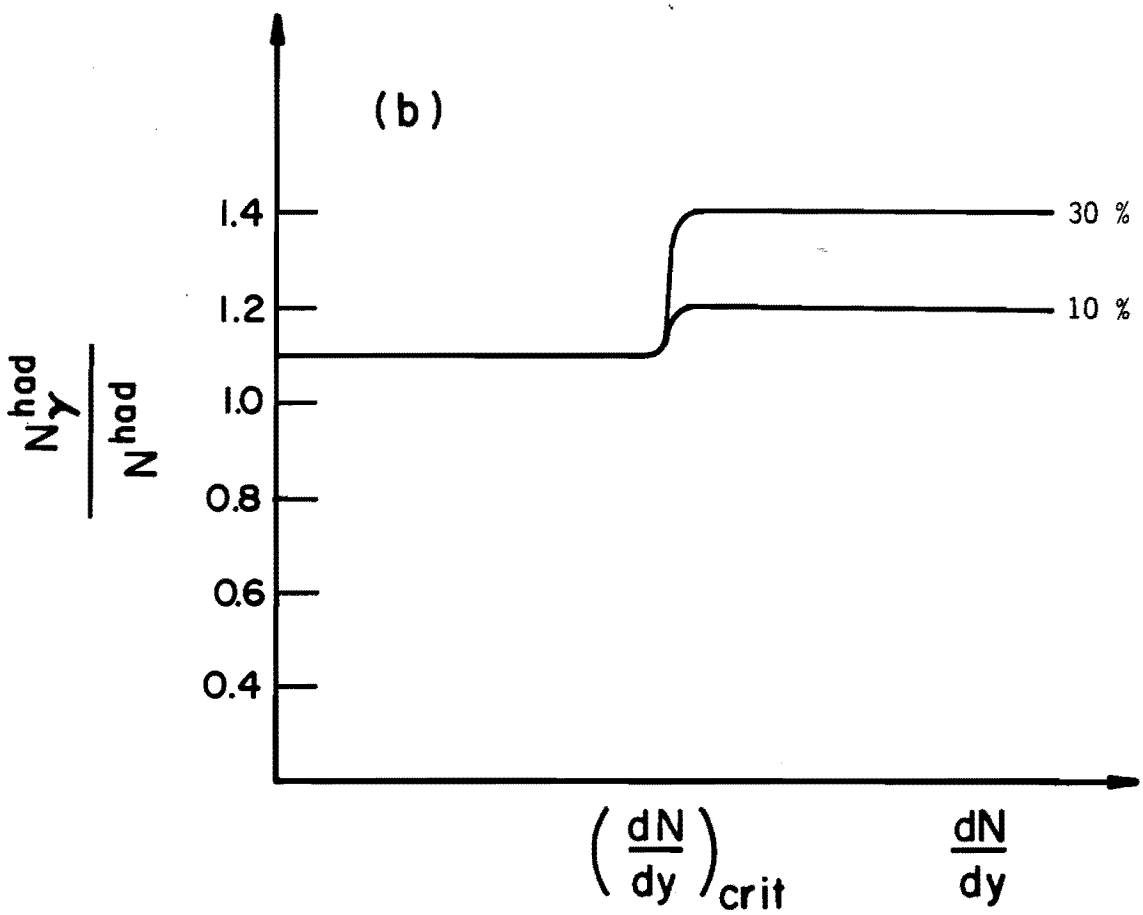
(b)
1.4
1.2
1.0
0.8
0.6
0.4
30 %
10 %
$\frac{N_\gamma^{had}}{N^{had}}$
$\left(\frac{dN}{dy}\right)_{crit}$
$\frac{dN}{dy}$

Fig. 10

and will be used as background subtraction from N_γ/N_{had} above the critical value of dN/dy.

We now discuss in more detail the properties of hadronic and direct photons.

1) γ's from hadron decay

The photons coming from hadron decays are a background to the direct photon signals but also are an important measurement in their own right. As was discussed in Section II.A., a measurement of the average transverse momentum of charged hadrons versus their density in rapidity space is important in a search for quark-gluon plasma formation. A measurement of the transverse momentum spectrum of γ's from π^0 decays contains similar information in that $\langle P_T^2\rangle_{\pi^0} = 3\langle P_T^2\rangle_\gamma - M_{\pi^0}^2/2$. In practice, of course, the γ acceptance is only partial, but we have verified that the $\langle P_T\rangle$ of the γ's entering our detector (See Section III.E.) leads to a good measure of $\langle P_T\rangle_{\pi^0}$. Figure 11 shows how the P_T spectrum of the detected decay γ's changes when the average π^0 transverse momentum is increased from 0.25 to 0.50 GeV/c (a parameterization of central π^0 production as measured at the ISR for charged pions was used). This information will therefore supplement the measured $\pi^\pm$ spectra. In fact, any deviation of the observed spectrum from that predicted for π^0 production (the average of π^+ and π^- production) would be evidence for additional sources of γ's. Figure 12 shows that the P_T spectrum of γ's from $\eta^0 \to \gamma\gamma$ decays would look similar to the γ spectrum from π^0 decays for large E_γ. The η^0 to π^0 cross section ratio of 0.3 used in Fig. 12 is the observed value at large transverse momentum.

2) Direct photons

The energy spectrum of the direct photons is determined by the production mechanism. If it is quark bremstrahlung then the energy spectrum is of $1/E_\gamma$

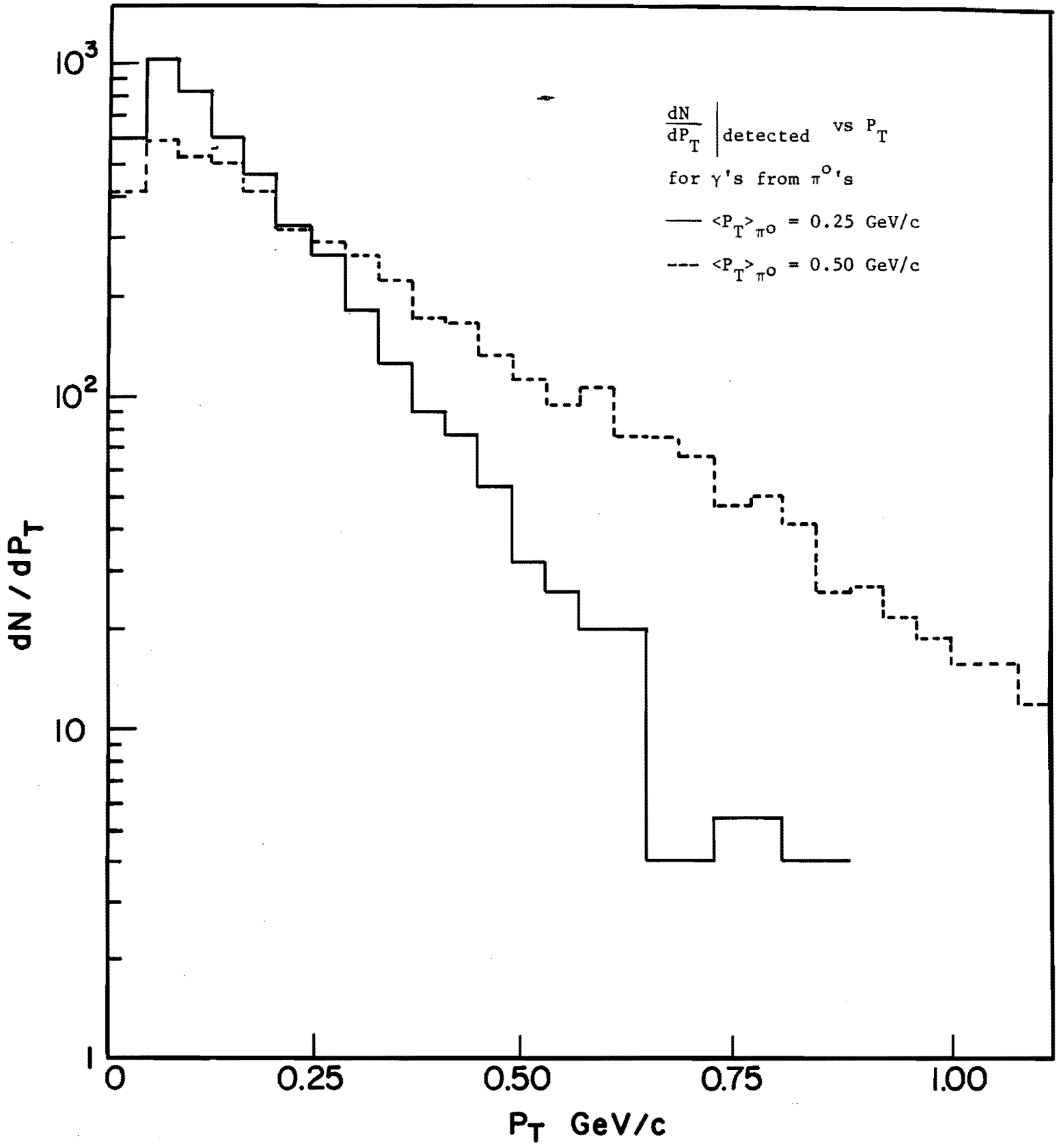
$\frac{dN}{dP_T}\Big|_{detected}$ vs P_T
for γ's from π^o's
—— $\langle P_T \rangle_{\pi^o}$ = 0.25 GeV/c
--- $\langle P_T \rangle_{\pi^o}$ = 0.50 GeV/c
10^3
10^2
10
1
dN / dP_T
0
0.25
0.50
0.75
1.00
P_T GeV/c

Fig. 11

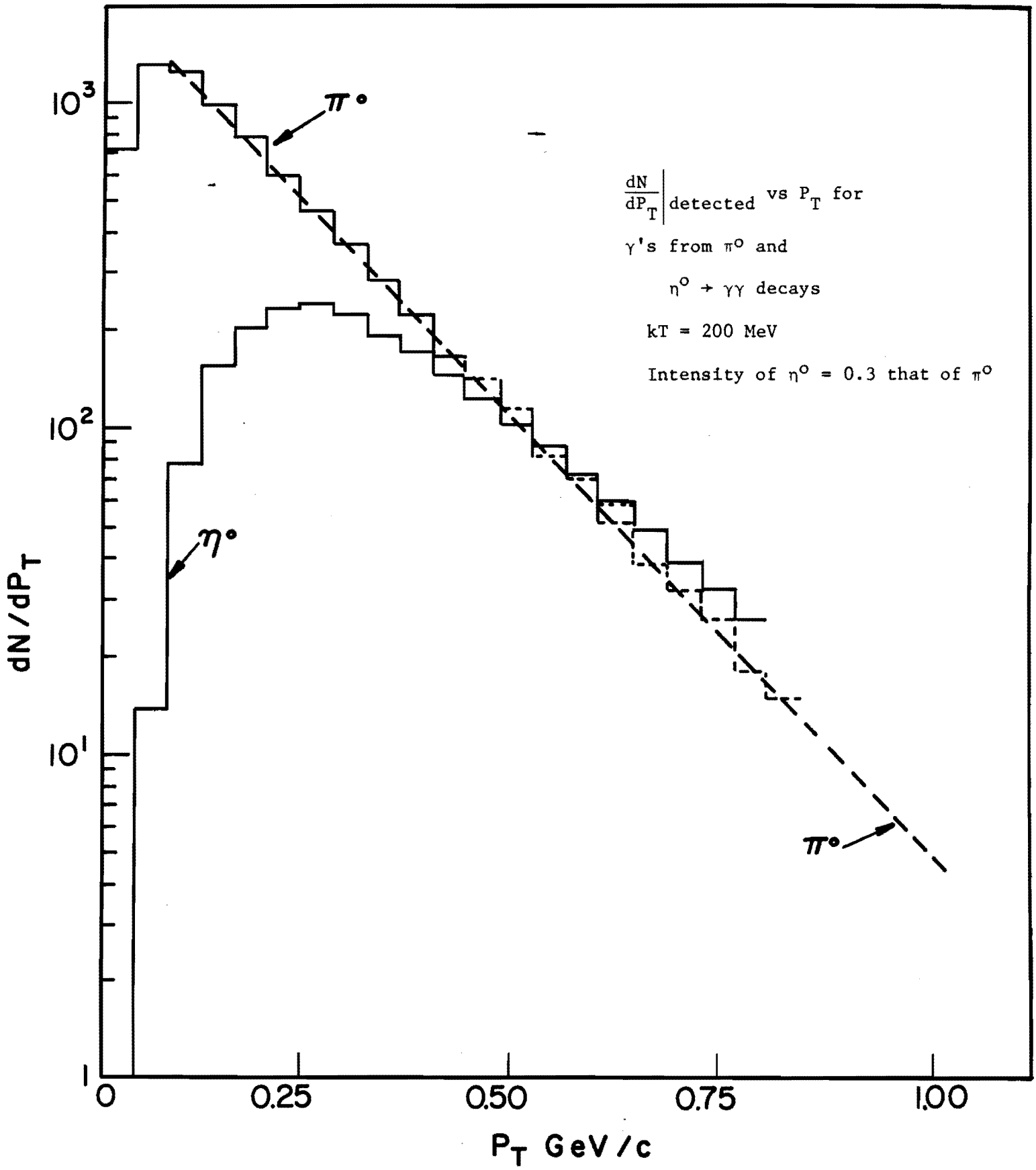
10^3
10^2
10^1
1
π°
η°
π°
$\frac{dN}{dP_T}\Big|_{\text{detected}}$ vs P_T for
γ's from π^o and
$\eta^o \to \gamma\gamma$ decays
kT = 200 MeV
Intensity of η^o = 0.3 that of π^o
dN/dP_T
0
0.25
0.50
0.75
1.00
P_T GeV/c

Fig. 12

form. The estimate of Ref. 22 is based on this picture. If however the photons are produced by quark-gluon Compton scattering

$$q + g \rightarrow q + \bar{\gamma}$$

the energy spectrum will tend to be closer to the black body spectrum with $T \simeq 200$ MeV. Due to the theoretical uncertainties we designed a broad band γ detector for the 20 MeV $\lesssim E_\gamma \lesssim$ 2 GeV regime.

C. Dileptons Emerging from a Quark-Gluon Plasma

An alternate electromagnetic signature would be the production of low mass lepton pairs. The mechanism is $\bar{q}q$ annihilation into leptons;

$$q + \bar{q} \rightarrow e^+ + e^- \quad .$$

The importance of this reaction for quark matter diagnostics has been discussed by Bjorken.[23] The cross sections for dilepton pairs will be suppressed by α^2 compared to the strong interaction rates. In a rough estimate that takes into account the thermal motion of quarks in the plasma, Domokos derives the temperature and invariant mass dependence of the dilepton production.[24] Using these formulae with $T \sim 200$ MeV, we estimate that 1 in 200 of events with $dn_c/dy \simeq 25$ will have a dilepton in the 200 - 600 MeV range of invariant mass. They are expected to be isotropic in the rest frame of the plasma and have a low ($m_{e^+e^-} < 600$ MeV) effective mass. Since this is the rarer of the two electromagnetic signatures, and because of space restrictions, we concentrate our experimental effort on measuring the direct photons.

D. Determination of the Size of the Centrally Produced Hadron System by the Hanbury-Brown and Twiss Intensity Interferometer Technique

As discussed in Appendix I the determination of the energy density (ε) requires the knowledge of the size (r) and lifetime (t) of the plasma, and the total energy emerging per unit rapidity (dE/dy), or in lieu of it the average energy per particle ($\bar{E}$) and multiplicity per unit rapidity (dn/dy);

$$\varepsilon = \frac{1}{t\pi r^2}\frac{dE}{dy} = \frac{1}{t\pi r^2}\frac{d\Sigma n_i E_i}{dy} = \frac{\bar{E}}{t\pi r^2}\frac{dn}{dy}$$

where we used the definition

$$\bar{E} = \frac{\sum_i n_i E_i}{\sum_i n_i} = \frac{\sum_i n_i E_i}{n} \quad .$$

Only those particles are summed which emerge in the rapidity interval dy. The multiplicity will be measured directly by our vertex detectors, the average energy by the spectrometer arms. To obtain t and r we have to perform the Hanbury-Brown and Twiss[25] analysis as applied to hadrons by Kopylov.[26] This method has been used successfully by us in a 28 GeV/c experiment.[27] It is based on measuring the distribution of transverse momentum difference q_t for like and unlike pion pairs, $p(q_t,q_o)$, and evaluate the ratio R

$$R^{\pm\pm}_{+-}(q_t,q_o) = \frac{p^{\pm\pm}(q_t,q_o)}{p^{+-}(q_t,q_o)}$$

when q_o denotes the energy difference between the ith and kth pion in an event

$$q_o = |E_i - E_k| \quad , \qquad q_t = \frac{|(\vec{p}_i+\vec{p}_k)\times(\vec{p}_i-\vec{p}_k)|}{|\vec{p}_i+\vec{p}_k|} = \frac{|\vec{s}\times\vec{d}|}{s} \quad .$$

The distribution $R^{\pm\pm}_{+-}$ has the form

$$R(q_t,q_o) = K\left[1 + \frac{I^2(rq_t)}{1 + (tq_o)^2}\right] .$$

As discussed in the introduction, with increasing dn_c/dy, the energy density ε will increase. Since the hadronization energy density ε_h is fixed and equal to the energy density of pions,[28] we expect that the hadronization volume will also increase as $\varepsilon/\varepsilon_h$ and thus r will grow as $(\varepsilon/\varepsilon_h)^{1/3}$. This increase has indeed been observed in a recent experiment[29] at the ISR. Since the correlation function depends on the product of r and q_t, with increasing r and thus multiplicity, the correlation as a function of q_t will shrink towards the origin. At a certain large value of the multiplicity the shrinkage will be so severe that the width of the correlation function will be comparable with the momentum resolution of our magnetic spectrometer, and thus the correlation pattern will not be observable. A sketch of the expected behavior is shown in Fig. 13 below. Assuming a 30 MeV/c momentum resolution, in the quantity $|(\vec{P}_i - \vec{P}_k)|$, we will be able to measure a hadronization volume up to r = 5 fm. This is larger than our estimate for the break up volume of the quark-gluon plasma and the energy density we will be able to detect.

The number of events that is needed to yield an error of 0.1 in the ratio R in the two dimensional (q_t,q_o) plane, and thus allow a determination of r and t for a given dn_c/dy, is twenty thousand independent events, where at least 2 pions pass through the magnetic spectrometer in each event. Assuming ten steps in dn_c/dy we need of the order of one hundred thousand <u>triggered</u> events. The emphasis on "triggered" refers to the fact that the natural abundance of high multiplicity events ($n_c = 5\ n_{max}$) is less by a factor of $\sim 10^4$ than the multiplicity of the most probable event, n_{max}.

Hanbury-Brown and Twiss

Hadronization Radius

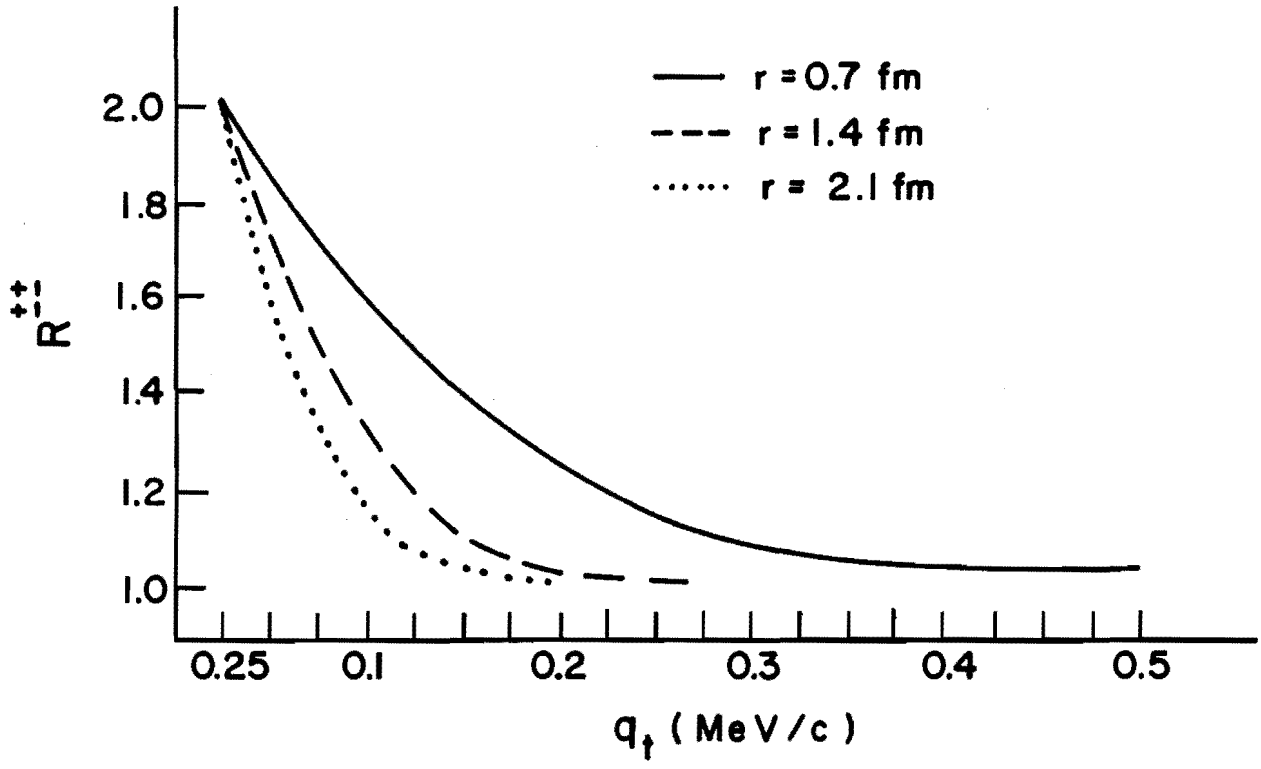

Fig. 13

To ensure that the spectrometer has the required momentum resolution we designed a spectrometer magnet with 50 MeV momentum transfer, and a 60 cm distance between the downstream end of the magnet and the third downstream chamber from the magnet. The drift chamber planes provide better than 0.4 mm spatial resolution. As the worst case, assume two tracks that emerge from the interaction vertex with the same angle but Δp = 30 MeV/c. The spatial separation at the last chamber will be 0.4 mm for a 600 MeV/c and 630 MeV/c pion, respectively. (Note that q_t can be zero even if the dipion emission angle is nonzero, thus our example is indeed the worst case situation.)

III. Experimental Design

A. Overview

The overall experimental layout is shown in Fig. 14 and Fig. 15. The $p\bar{p}$ interaction region which extends for $\sim$ 50 cm along the collider axis is surrounded by a central cylindrical drift chamber which covers $|y| \lesssim 2$ and end caps which cover $2 \lesssim |y| \leq 3$. This system is covered by a single layer hodoscope which is used in a fast nanosecond trigger. Minimum-bias trigger counters are not shown in the figures.

A single arm magnetic spectrometer with time-of-flight for particle identification samples the high multiplicity events. Scintillation glass array #1 which completes the spectrometer, measures the gamma rays and tags the charged particles which traverse the spectrometer. The ability of the central chamber to determine the vertex of the multiparticle event is improved by the second set of "z" chambers which are oriented $\sim 120^{o}$ with respect to the median plane of the spectrometer (see Fig. 15).

Scintillation glass array #2 is located directly underneath the central cylindrical drift chamber. The much larger solid angle of this array will permit detection of events with multi photon production. A more detailed discussion is given in the following sections.

B. Central Drift Chamber

The measurement of the number of charged particle N_D is accomplished using a central cylindrical drift chamber and two end cap chambers as shown in Fig. 14. The central drift chamber has an inner radius of 20 cm and an outer radius of 40 cm and is 2 meters long.

TOP VIEW OF SPECTROMETER

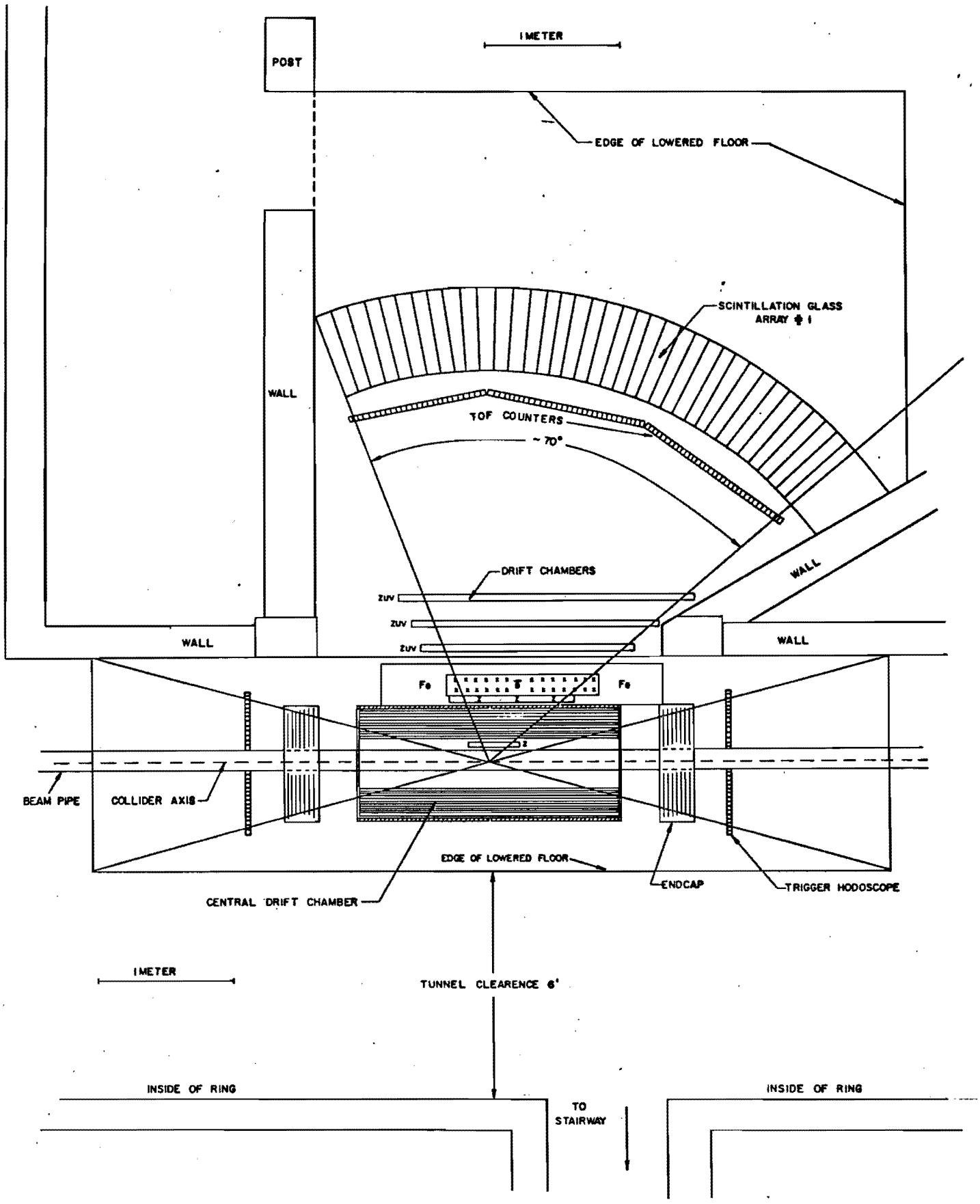

Fig. 14

SIDE VIEW OF SPECTROMETER (LOOKING UPSTREAM)

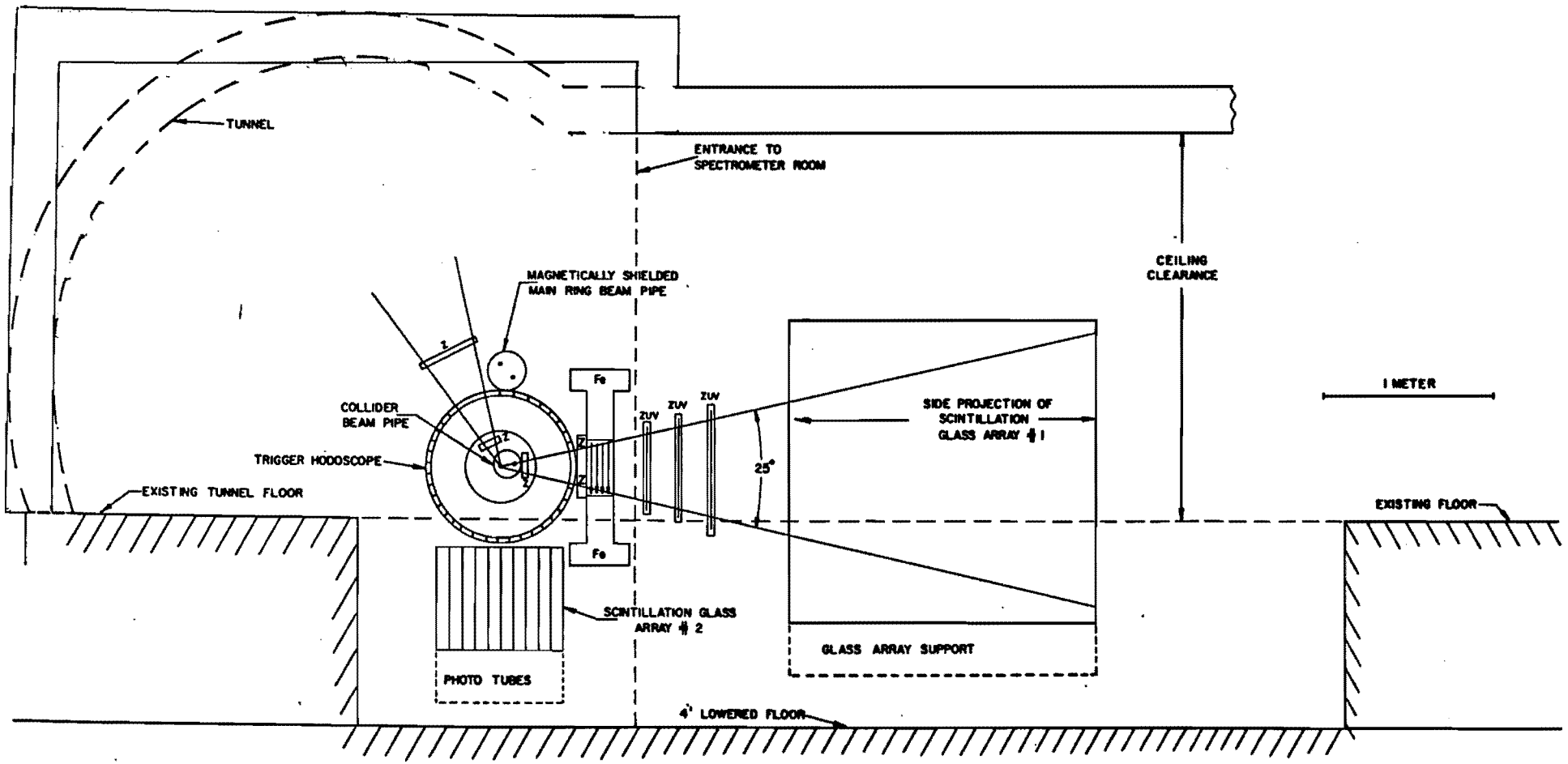

Fig. 15

We propose to use the "JADE" type drift chamber developed at DESY and Heidelberg.[30-33]. In addition to its proven capability for efficient tracking of high multiplicity events, a "JADE" chamber minimizes the total amount of mass (we will operate at 1 atmosphere pressure) in the central tracking chamber and hence the probability of secondary interactions. Since we will operate at high multiplicity and one of the physics objectives involves soft photons, this property of the chamber is highly desirable. A cross section of one of the 24 drift chamber cells is shown in Fig. 16. The two meter long sense wires run paralled to the beam axis. A charged particle traversing the drift cell would produce up to 16 hits in the chamber. The z coordinate along the chamber axis is obtained by charge division. The left-right ambiguity is eliminated by staggering the azimuthal position of alternate sense wires by ±150 μ and comparing the total drift times.

Each cell has a multi-hit capability (8 hits) based on a sampling time of ∿ 80 nanoseconds for charge accumulation.

Since we expect to see events as high as $\frac{dn_c}{dy} = 20$ and the chamber covers $|y| \leq 2$ in rapidity we must be able to identify 80 tracks. The chamber can detect up to 24 x 8 = 192 tracks if they are isotropically distributed.

The chamber can be constructed to minimize the mass that the particles traverse. The mechanical construction using Aluminum reinforced Rohacell would present about 0.01 radiation lengths to the charged particles. The saver beam pipe mass must also be a minimum. A 25 mil wall thickness Beryllium tube would have a radiation length of less than 0.005. The original JADE chamber which also used charge division to measure $\frac{dE}{dx}$ was operated at four atmospheres.

"JADE" DRIFT CHAMBER CELL

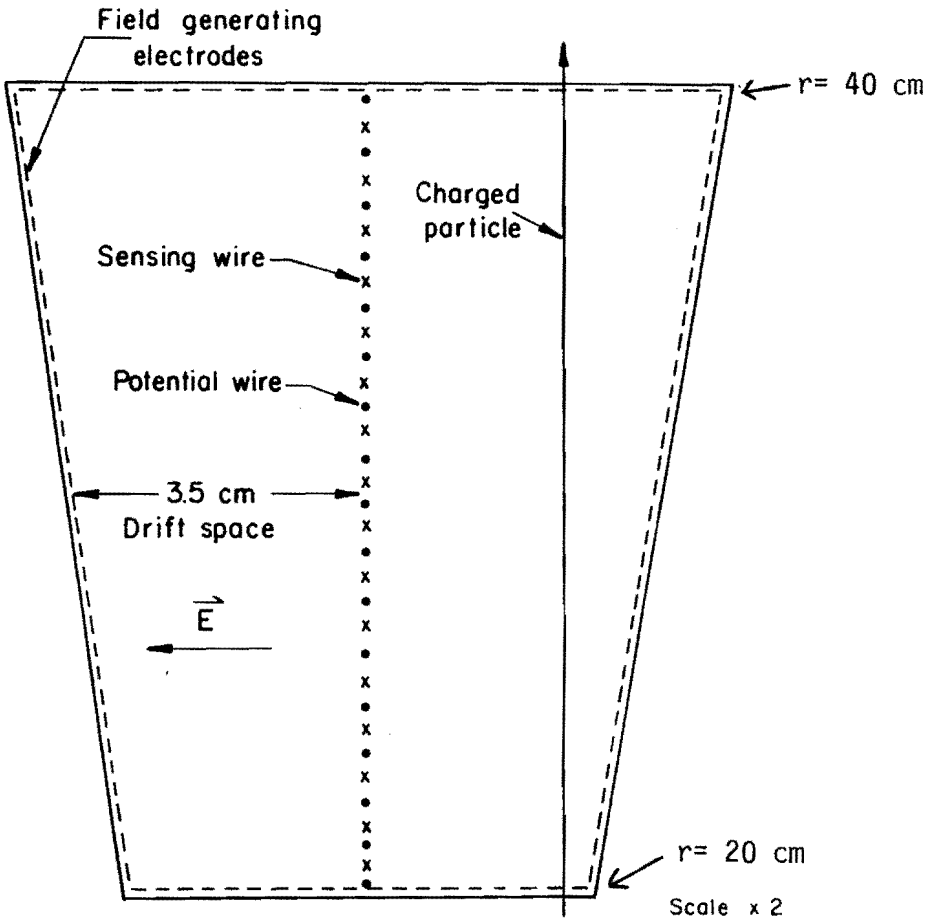

24 Required for central chamber

Fig. 16

$\frac{dn_c}{dy}$	$\Delta\left(\frac{dn_c}{dy}\right)$	N_{cdc}	$\Delta\left(N_{cdc}\right)$
3.5	±0.5	13.4	±2.5
20	±1.5	77	±7.7

The most severe requirements on track recognition accuracy in the central drift chambers are set by the desire to measure dn_c/dy vs $\langle P_t \rangle$ (Fig. 6). In the above table we list the extremes of dn_c/dy along with the number of tracks in the central chamber (N_{CDC}) and the required precision (ΔN_{CDC}). The desired precision of ± 10% for large N_{CDC} appears achievable.

Our chambers would have to be operated at one atmosphere which would reduce the charge division accuracy, however, we are dealing with straight tracks. We are also investigating the use of Xenon gas which would triple the basic $\frac{dE}{dx}$ sensitivity of the chamber. This could be practical if our chamber does not require constant gas recirculation. The DESY experience suggests that a JADE chamber can be run in a sealed off mode over a period of many weeks.

Cost

24 sections each with 16 wires = 384 wires

Electronics @ $400/wire.	$154, K
Mechanical @$200/wire	$77K
	$231 K

C. End Cap Drift Chambers

Two designs for end cap drift chambers are being considered. Both designs occupy the same space, cover the same rapidity range, and have a "bicycle wheel" structure. An end cap chamber begins 50" from the intersection center and ends 60" from the center. The sensitive region extends radially 6" to 18" from the saver beam line. This provides full tracking with all 6 wire planes for $1.92 < |y| < 2.88$. For $|y| < 1.92$ the central drift chamber provides ≥ 8 points on a track, so there is a comfortable overlap between the central and end cap regions.

An end cap plane contains thirty $\times 12^{o}$ segments (See Fig. 17), each with a "spoke" for measuring drift time. Drift time is normally normally 1 microsec at the outer radius and 300 nsec at the inner radius, well within the time between beam crossings. KNO-scaling events with charged multiplicities of 200 near the useful extreme of our luminosity limitations, will produce

about 25 tracks in these 30 segments. Multi-hit capability is included for the electronics of both designs.

Design I

The sense spoke consists of a delay line (1.67 ns/cm) at ground potential with positive potential sense wires spaced 2mm on either side of the delay line. This signal induced on the delay line is detected with a differential smplifier. Except for the 4 mm between the 2 sense wires, left-right ambiguity can be resolved by detecting either the polarity of the delay line pulse or which sense wire was hit. Polarity sensing makes it easier to handle multi-hit cases. A unique r-ϕ cooridinate is obtained with each hit. Delay position should be measurable to 5 mm with 1 ns TDC's, and drift distances measurable from 200 μm to 500 μm. Double hit capability applies for pulses more than 10 ns apart.

Cost

12 planes (360 spokes)--	
2 TDC's per spoke--720 TDC's @ $35 each	$ 25 K
Amplifiers and discriminators	$ 8K
Ribbon and Connectors	$ 15K
Fastbus Crate	$ 5K
Mechanical Construction (Including Overhead)	$ 100K
	$ 152K

Design II

The sense spoke consists of a single sense wire at ground potential. Charge division provides the radial coordinate with 3-6 mm accuracy. Sense wires in successive planes must be staggered ±150 μ to resolve left-right ambiguities. Electronics will be the same as used with JADE chambers, giving multi-hit capability for pulses more than 85 ns apart. Costs per wire are estimated to be $400 electronics and $200 mechanical. An advantage of this system is that the electronics would be the same as that used for the central chambers.

Cost

Electrical (360 spokes)	$144K
Mechanical	$ 72K
	$216K

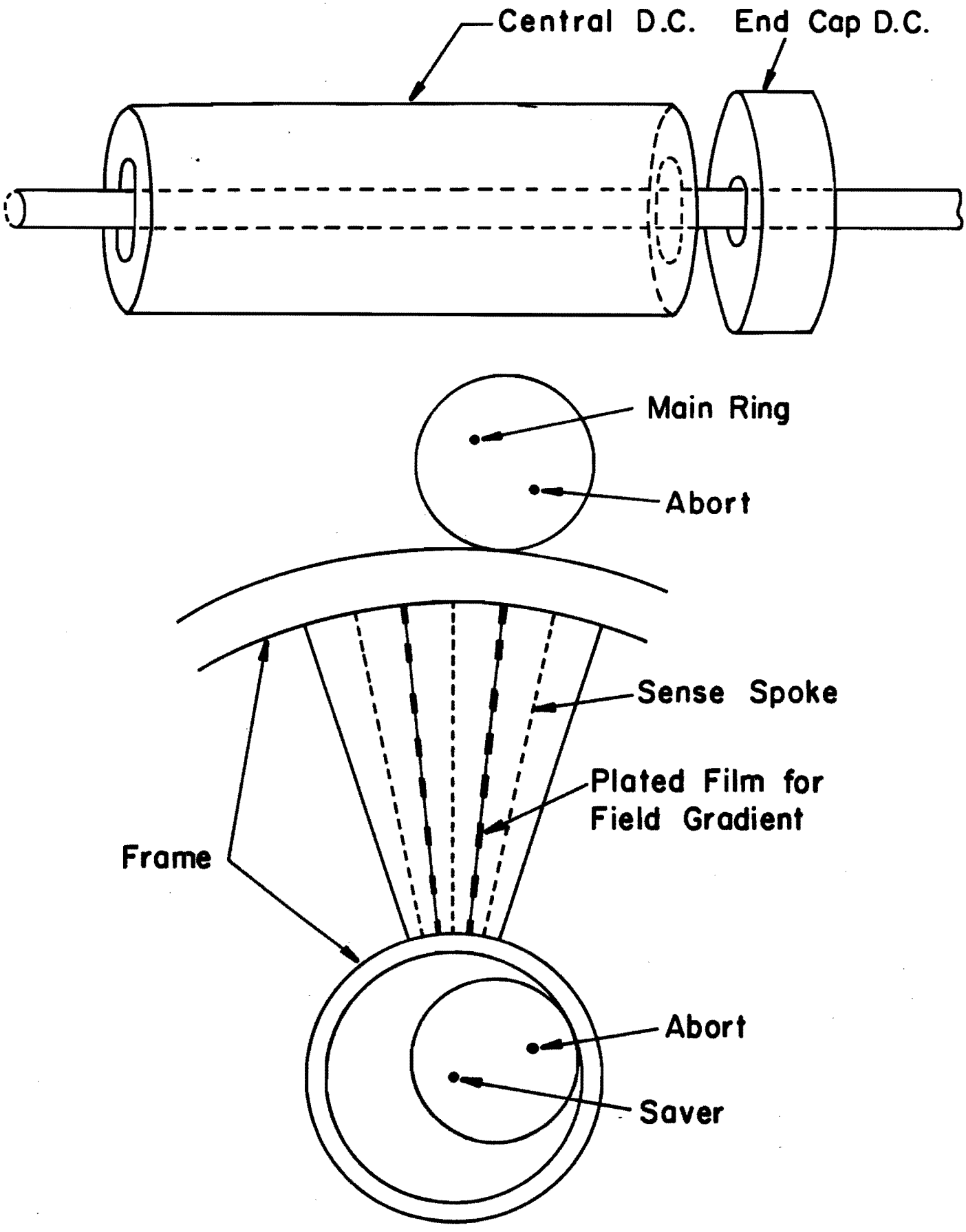
Central D.C.
End Cap D.C.
Main Ring
Abort
Sense Spoke
Plated Film for
Field Gradient
Frame
Abort
Saver

Fig. 17

D. The Low Momentum Spectrometer

The layout of the low mementum spectrometer is shown in Figs. 14 and 15. The design is traditional and has a rapidity acceptance which covers the y interval from + 0.4 to - 1.0 and a azimuthal acceptance of 25^{o}. For a most probable charged multiplicity, n_{max} = 28, the probability of acceptance is 0.35 particles.

The magnet will be built of conventional upper coils and iron return path, with 48" by 12" gap. The full set of design parameters are given in Appen. III. The design ensures that adequate homogenity of the B field is obtained and that uncertainties in the fringe field do not interfere with the event reconstruction.

Three drift chambers determine the incident particle direction and three drift chambers behind the magnet determine the final direction. The transverse momentum kick is 50 MeV/c, and the momentum uncertainity dp/p in % is $dp/p = \sqrt{(1.5)^2+(3p)^2}\%$ (with p in GeV/c).

Time flight is measured by a 1.5 m by 3.0 m hodoscope located about 3 m from the interaction region (adjustable in the range 1.5 to 3.0 meters.) Pions, kaons and protons will be separated in the 0.3 to 1.4 Gev/c range by a time of flight measurement with a time resolution of 0.4 ns. With a flight path of 3 meters the time of flight for the various particles are shown in Table 1. Fig. 18 (a) shows the probability of a charged kaon surviving a flight path L of 1.5 m and 3.0 m respectively and Fig. 18 (b) shows the difference in time of flight between pions and kaons for the two TOF distances as a function of momentum. Considerations based on the experimental distribution dN/dp at 0.5 TeV (see Fig. 9) and the

Bose-Einstein curve with T = 200 MeV, suggest that the interesting region of momentum extends from 0.1 GeV/c to 1.4 GeV/c. Inaccessible are kaons in the momentum region 0.1 to 0.3 GeV/c which are too short lived to survive (See Fig. 20).* We are able to explore th region either with two settings of the TOF path length (1.5, 3.0 m) (or with a single path length of 2.0 m).

The expected performance of this spectrometer is in line with the published results of our ARGO spectrometer[34] and the CERN UA2[14] spectrometers. The two drift chambers which are inside the central drift chambers which we refer to as "Z-chambers" or "prechambers" (see Fig. 15) are used to determine the vertex of the interaction along the z-direction which is parallel to the beam. One of these a 100 x 8.25 cm unit is located in the spectrometer arm and a second 100 x8.25cm unit looks in from above. The low mass design is illustrated in Fig. 20. It consists of three layers in Zuv configuration. The estimated costs for all of four Z chambers is shown below.

length (cm)	width (cm)	wire spacing (cm)	number of wires (3 planes)
100	8.25	0.4	750
100	8.25	0.4	750
120	30	1	360
240	30	1	720

Total number of wire = 2580

Cost 2580 @ \$70/wire = \$ 181K

* The total mass encountered by a particle traversing the spectrometer is estimated to be about 1 gm/cm^2. This means that there is a low momentum cut off for pions, kaons, and protons. The cutoff values for a 2 gm thickness is shown below:

	pions	kaons	protons
Range	75 MeV/c	185 MeV/c	295 MeV/c

Table 1

TIME OF FLIGHT FOR 3 METER PATH

P	TOF			DELTA T				
	e	π	K	P	P-π	P-K	K-π	π-e
GeV/c	nanosec							
0.1	10.0	17.2	50.4	94.4	77.2	44.0	33.2	7.2
0.2	10.0	12.2	26.7	48.0	35.8	21.3	14.4	2.2
0.3	10.0	11.0	19.3	32.9	21.8	13.6	8.2	1.0
0.4	10.0	10.6	15.9	25.5	14.9	9.6	5.3	0.6
0.5	10.0	10.4	14.1	21.3	10.9	7.2	3.7	0.4
0.6	10.0	10.3	13.0	18.6	8.3	5.6	2.7	0.3
0.7	10.0	10.2	12.2	16.7	6.5	4.5	2.0	0.2
0.8	10.0	10.2	11.8	15.4	5.3	3.7	1.6	0.2
0.9	10.0	10.1	11.4	14.5	4.3	3.0	1.3	0.1
1.0	10.0	10.1	11.2	13.7	3.6	2.6	1.1	0.1
1.1	10.0	10.1	11.0	13.2	3.1	2.2	0.9	0.1
1.2	10.0	10.1	10.8	12.7	2.6	1.9	0.7	0.1
1.3	10.0	10.1	10.7	12.3	2.3	1.6	0.6	0.1
1.4	10.0	10.1	10.6	12.0	2.0	1.4	0.6	0.0
1.5	10.0	10.0	10.5	11.8	1.8	1.3	0.5	0.0

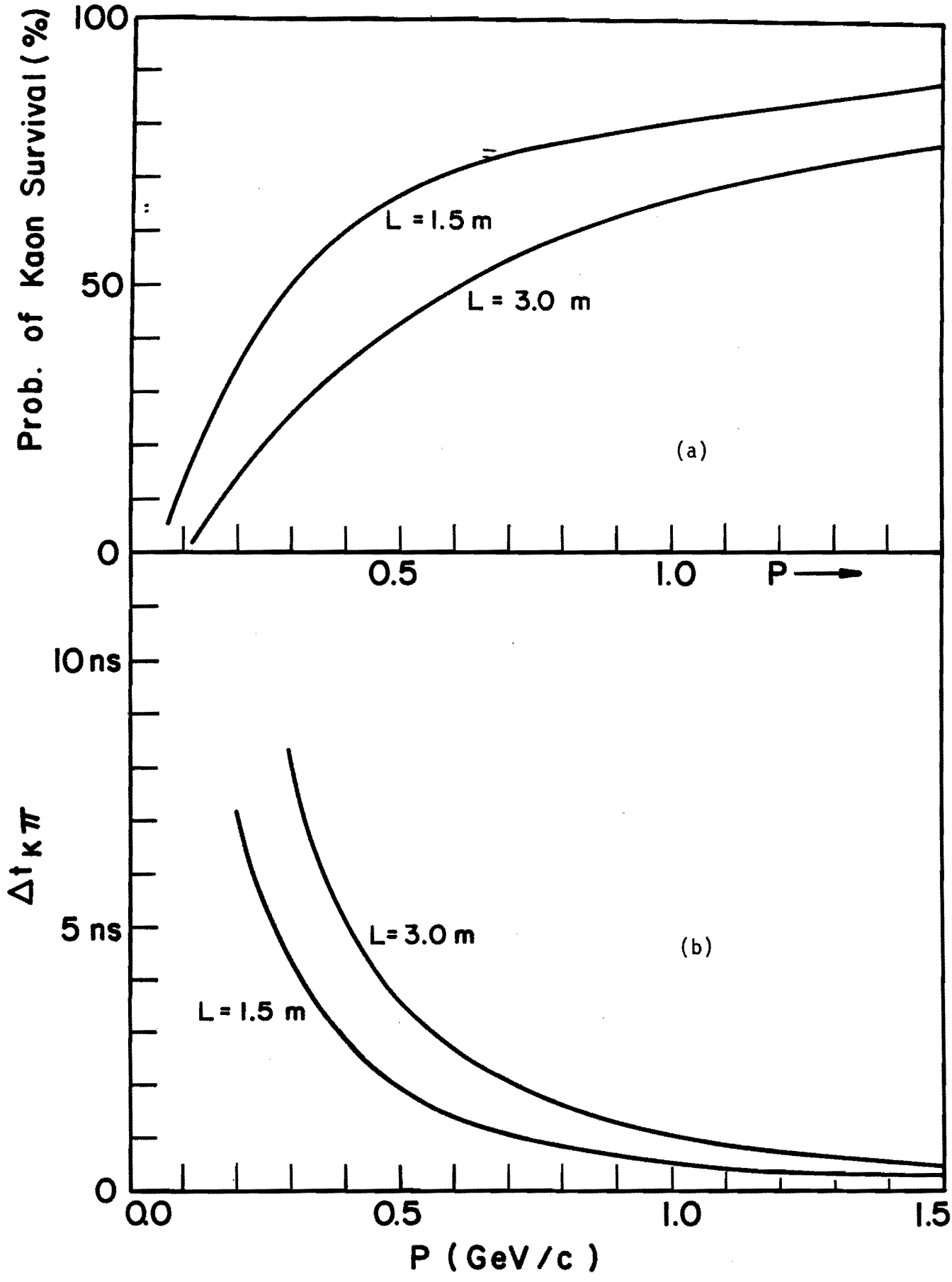
Prob. of Kaon Survival (%)
100
50
0
L = 1.5 m
L = 3.0 m
(a)
0.5
1.0
P
10 ns
5 ns
0
$\Delta t_{K\pi}$
L = 3.0 m
L = 1.5 m
(b)
0.0
0.5
1.0
1.5
P (GeV / c)

Fig. 18

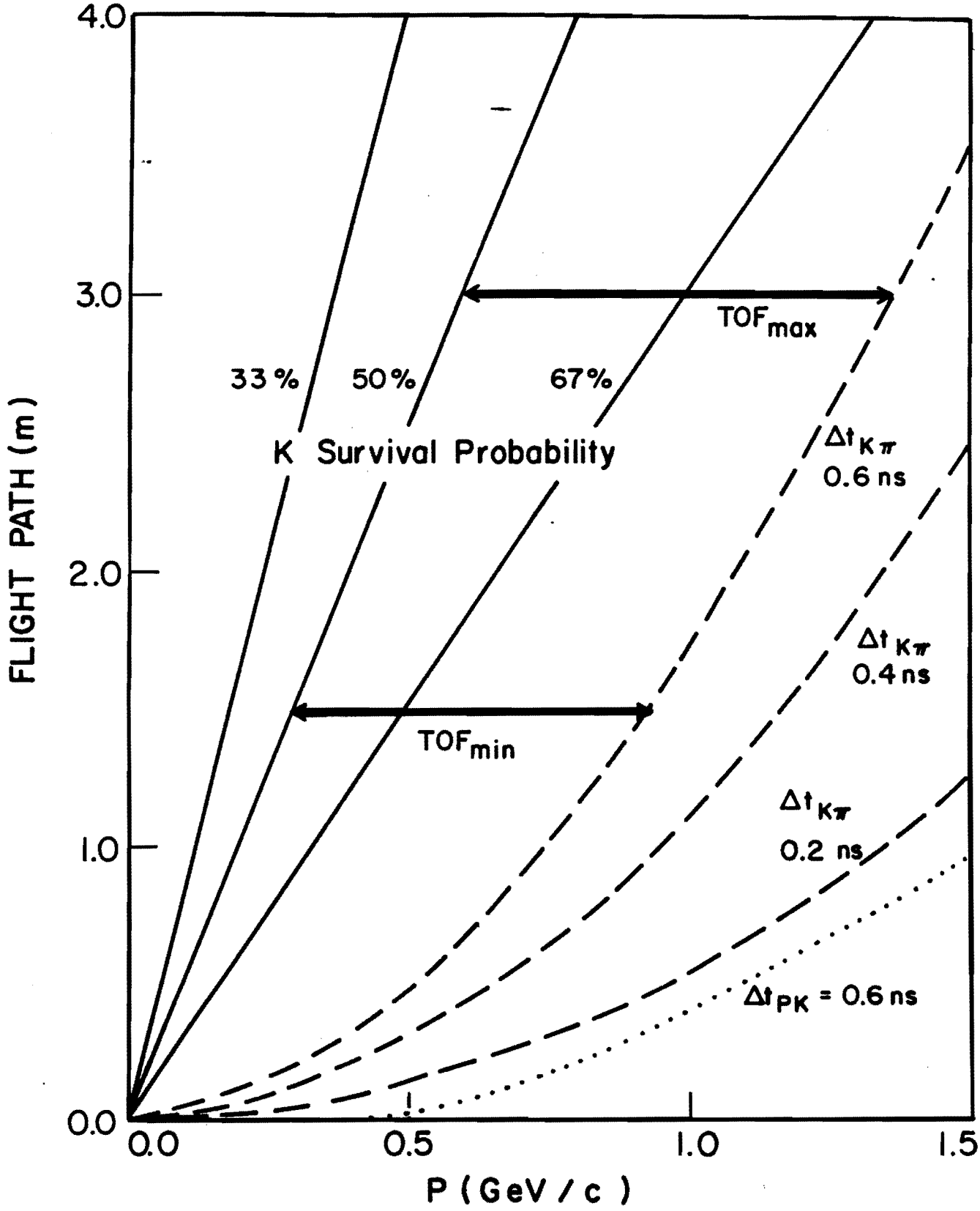
4.0
3.0
2.0
1.0
0.0
FLIGHT PATH (m)
0.0
0.5
1.0
1.5
P (GeV / c)
33 %
50 %
67 %
K Survival Probability
TOF max
TOF min
Δt Kπ
0.6 ns
Δt Kπ
0.4 ns
Δt Kπ
0.2 ns
Δt PK = 0.6 ns

Fig. 19

Z CHAMBER FRAME

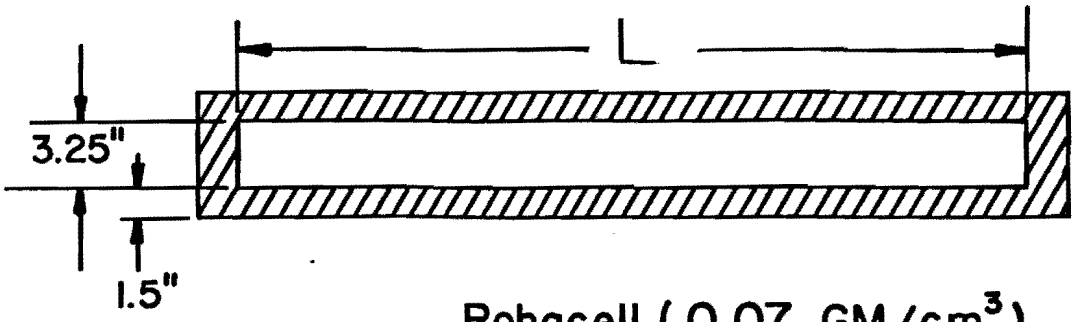

1" = 0.1"

Rohacell (0.07 GM/cm^3)

Prestressed

0.2" thick

CHAMBER EDGE VIEW

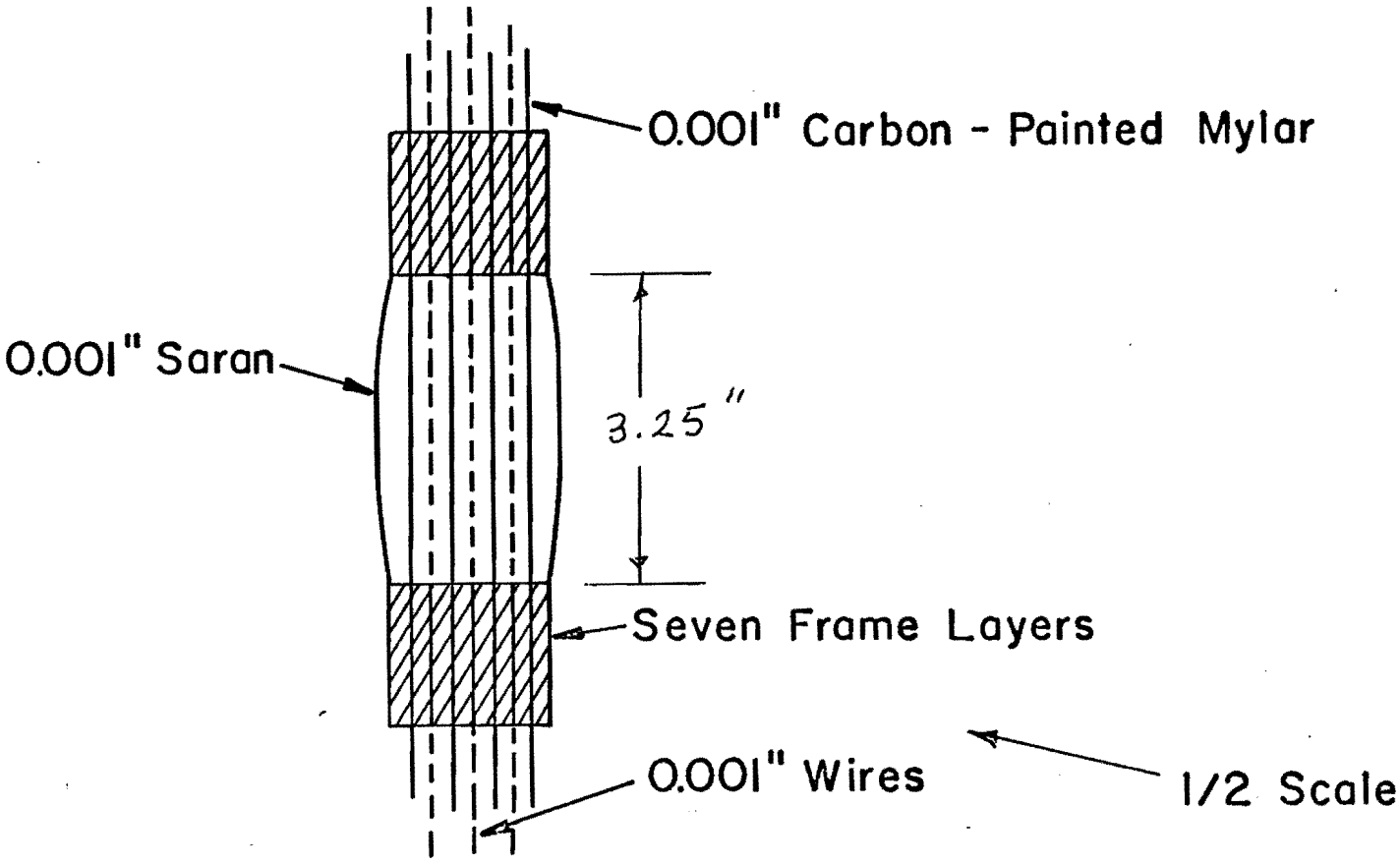

Fig. 20

E. Photon Detection

The photon detector array #1 is shown in Fig. 14. The array defines the same solid angle as the charged particle spectrometer 70° horizontally and 25° vertically ($\Delta\Omega$ = 0.53 Sr). We want to measure γ energies from 20 MeV up to a few GeV and tag charged particle tracks entering the spectrometer. The photon detector array #1 is composed of segmented scintillation glass cells which point toward the center of the interaction region. Scintillation paddles behind the glass would be used to detect punch throughs from neutral hadron interactions.

The energy resolution of this detector is expected to be

$$\frac{\sigma_E}{E} = 1\% + \frac{1.5\%}{\sqrt{E(GeV)}}$$

for

$$E_\gamma > 200 \text{ MeV} .$$

For lower energy γ rays, 20 MeV < E_γ < 200 MeV

$$\frac{\sigma_E}{E} = 1\% + \frac{3\%}{\sqrt{E(GeV)}} .$$

The latter resolution figures are based on a KEK measurement[35] using 20 to 190 MeV electrons. Hence for 20 MeV γ's

$$\frac{\sigma_E}{E} \simeq 20\% .$$

We will make a time of flight measurement of the photons from the interaction region to discriminate background photons and non-relativistic neutral hadrons. Scintillation glass has a light decay time of τ = 70 ns.

We are exploring the possibility of using leading edge timing of the scintillation light. A time resolution of ~ 1 ns would allow us to identify photons whose flight path was 1 foot longer than the direct path.

In this array an individual cell would have a front surface of 10 cm × 10 cm, a back surface of 13 cm × 13 cm and have a length of 60 cm (14 radiation lengths). This array would have an angular resolution of ±7 mrad. The spherical array consists of 37 horizontal and 13 vertical blocks.

In comparison with photon detector #2 this detector will do a much better job of measuring the γ energy spectrum for two reasons. It has a better geometry for an extended ~ 50 cm interaction region and it can discriminate against background counts using time of flight.

Cost

Photon Detector Array #1

481 Blocks	@ $1301	$ 626K
481 Phototubes	@ $350	$ 169K
481 ADC's	@ $100	$ 48K
Supporting frame		$ 50K
Cables		$ 10K
		$ 903K

Photon detector array #2 is located directly underneath the cylindrical drift chamber and subtends a larger solid angle of $\Delta\Omega$ = 1.2 sterradian. The present design is a flat array consisting of segmented scintillation glass cells whose front surfaces are 7 cm × 7 cm and whose length is 60 cm (14 radiation lengths). The array is 10 cells wide by 20 cells long.

Array #2 serves two functions. (a) We can verify that the transverse electromagnetic energy deposited in array #2, just as the transverse hadronic energy, increases with n_c. (b) –Due to its larger solid angle it can detect multiphoton production in a single event. This will be important for the detection of the quark-gluon plasma.

Cost

Photon Detector Array #2

200 Blocks	@ &750.	$ 150K
200 Phototubes	@ $350.	$ 70K
200 ADC's	@ $100.	$ 20K
Supporting frame		$ 10K
Cables		$ 5K
		$ 255K

F. Trigger Considerations

A single layer scintillation hodoscope backs both the central drift chamber and the two end caps. The hodoscope consists of 136 elements around the central chamber and 100 elements on both end caps for a total of 236 elements. In addition, minimum bias triggers are located further upstream and downstream from the interaction region. (Not shown.) A fast nanosecond trigger for a multiparticle event n_c would select out events whose transverse momentum is ~ 0.6 GeV/c $\times n_c$ where n_c is the total charged particle multiplicity. Since the hodoscope covers the rapidity values $|y| \leq 3$ only about half of the produced particles pass through our detectors. Thus we would be able to use only about half of the charged particles ($n_c/2$) in the trigger.

Thus a high multiplicity trigger would select out the most interesting events. That is, $n_c/2 = 40$ would correspond to a transverse energy of 48 GeV. Of course this multiplicity trigger could be augmented by requiring at least one charged particle or γ ray in the time of flight spectrometer.

It should be possible to include information from the central drift chambers and the end caps in a second level trigger which would require up to one microsecond after the $p\bar{p}$ collision. Although we are primarily interested in events where $n_c >> \bar{n}_c$ and that are isotropic in the laboratory, the second level trigger would permit early identification of other events which exhibit anisotropic particle distributions.

IV. Data Collection Rate

In order to estimate the numbers of events to be recorded as a function of n_c we will use the multiplicity distribution observed at $\sqrt{s}$ = 0.5 TeV by the UA5 apparatus (See Fig. 7) and assume that KNO scaling holds to very high values of n_c at $\sqrt{s}$ = 2 TeV. Since the $\bar{n}_c$ should scale according to

$$a_0 + a_1 \ln s + a_2 \ln s^2 \quad ,$$

at $\sqrt{s}$ = 2 TeV we expect $\bar{n}_c$ = 35. KNO scaling predicts the most probable multiplicity, n_{max} is 0.8 $\bar{n}_c$ = 28, and that the cross section drops about one order of magnitude for every multiple of $n_c/\bar{n}_c$ thus one event in every 10^5 should have 200 charged particles.

We assume that $n_c = n_{max} = 28$ and an inelastic cross section of 40 mb. In Table II we give the events per day and the events for a 3 month run as a function of n_c. We have used the spectrometer acceptance described in Section III.D. and have corrected for the probability that no charged particle will enter the spectrometer.

The conclusion is that a luminosity of $(\frac{1}{73}) \times 10^{+30}$ cm^{-2} sec^{-1} (at C_0 $\beta^* = 73$ meters as compared to $\beta^* = 1$ meter at B_0) will provide this experiment with a data sample of 40,000 events having $n_c \geq 200$ and with one or more particles in the side spectrometer. Given the steepness of the KNO curve, it is clear that an even lower luminosity of 10^{+27} cm^{-2} sec^{-1} would provide a valuable data sample. It is also clear from Table II that we must heavily scale down the number of events accepted at low n_c in order to limit the data base to a manageable number, e.g., 2×10^6 events.

TABLE 2

Normal KNO Events

N_{charge}^{true}	Relative σ^N	N_{charge} $\Delta\theta = 70°$ $\Delta\phi = 25°$	Events/Day with at least one track	Events per 3 months
27.6	1	.27	1.1×10^7	$.9 \times 10^9$
62.0	10^{-1}	.60	1.9×10^6	1.0×10^8
97.6	10^{-2}	.95	2.4×10^5	2.1×10^7
131.0	10^{-3}	1.28	2.7×10^4	2.4×10^6
166.0	10^{-4}	1.62	2.9×10^3	2.6×10^5
200	10^{-5}	1.96	3.0×10^2	2.8×10^4

$$\text{Luminosity} = \left(\frac{1}{75}\right) \times 10^{30}$$

$$\sigma^{\text{inelastic}} = 40 \text{ mb}$$

V. Experimental Area Considerations

A. Area Layout

A top view of the experimental area is shown in Fig. 21. The principal feature is the pit area which extends from the tunnel area into the spectrometer room. The pit area in the tunnel extends ±3 meters from the beam collision point which is well away from the room temperature magnets which are located 4 meters upstream and 9 meters downstream. The design provides for a 6 ft clearance for magnet vehicle transit. The four foot depth of the pit allows the construction of a horizontal charged particle spectrometer. Consequently the photon detector array #1 is a vertical stack. Because of weight considerations this is an important feature. The pit also permits the installation of a large solid angle scintillation glass array under the central cylindrical drift chamber. Volume of the pit area ~ 50 cubic yards (c.y.).

Cost Estimate of Pit

Based on 50 c.y.

Break Out Concrete - 50 c.y.	$400	$ 20,000
Hauling - 50 c.y.	$40	$ 2,000
Shoring - 40 c.y.	$700	$ 28,000
Flooring - 50 c.y.	$700	$ 35,000
Drainage Revision.		$ 15,000
Elect. Revision.		$ 15,000
Misc.		$ 25,000
		$ 140,000

TOP VIEW OF CO PIT AREA FOR P-735

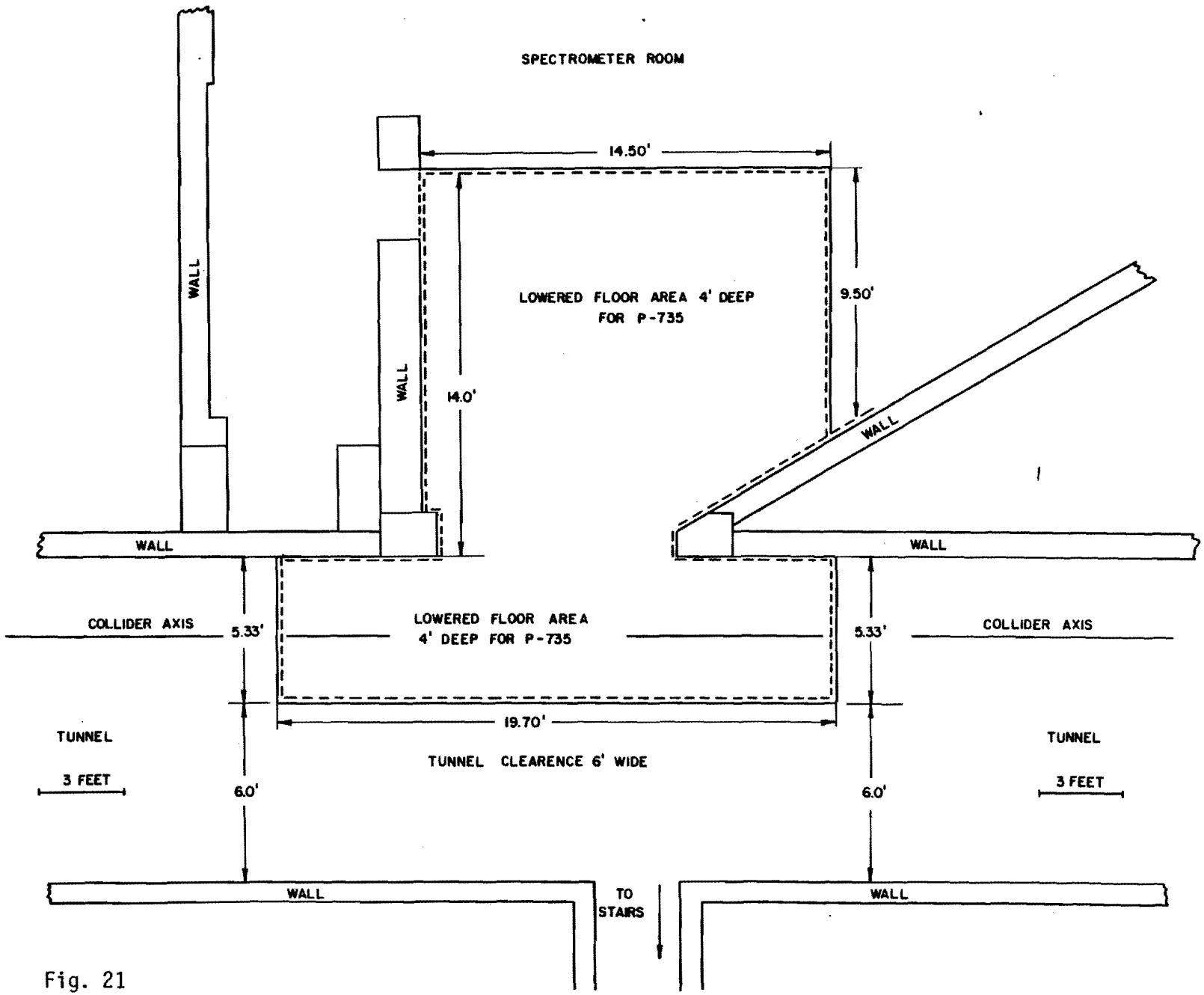

Fig. 21

B. Spectrometer Magnet Fringe Field Effects on the Accelerators

As seen in Fig. 15, the Tavatron beam orbit is in the median plane of the spectrometer magnet (See Fig. 22 and Appendix 3 for magnet parameters) and displaced 24.5 inches from the magnet center. For a central field of 3.6 kg, a first-order LINDA calculation[37] indicates a vertical field of 120 g at the Tevatron beam, extending for 1.5 m along the beam. A quadrupole field of 20 g/in over a similar path length is present also. The spectrometer magnet will be on only when the Tevatron beam is at full energy. At a beam energy of 1 TeV, we estimate that the dipole fringe field will make a 0.25 mm perturbation in the horizontal closed-orbit and the quadrupole fringe field will make a tune shift of 2×10^{-4}. Both effects appear to be small; the closed orbit perturbation could be easily compensated with a single nearby dipole.

The same LINDA calculation gives a fringe field at the Main Ring beam orbit (25.5 in above the Tevatron orbit) of 120 g. This would have detrimental effects on the Main Ring beam, particularly at the 8 GeV injection level. This field will be shielded out by placing ~ 0.5" of magnetic shielding around the Main Ring beam pipe for a distance of ±1.5 m adjacent to the spectrometer magnet.

P-735 SPECTROMETER MAGNET

B_{MAX} = 3.6 KG

$\int B dl \Longleftrightarrow$ 50 MeV/c

P_{MAX} = 60 KW

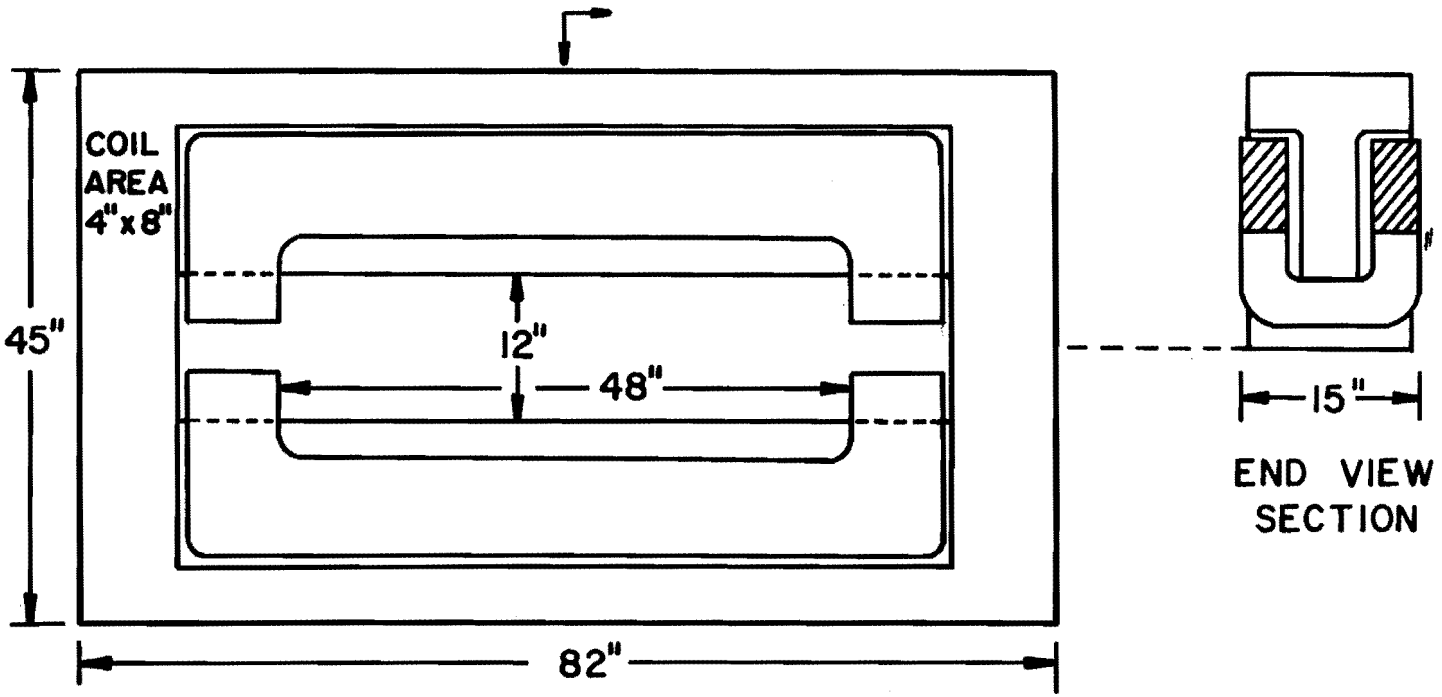

SIDE VIEW

END VIEW
SECTION

Fig. 22

VI. Cost Estimate Summary

1. Central Cylindrical Drift Chamber

24 sections each with 16 wires = 384 wires

Electronics @ $400/wire	$ 154K
Mechanical @ $200/wire	$ 77K
	$ 231K

2. End Cap Drift Chamber

30 sections each with 12 wires = 360 wires

Electronics @ $400/wire	$ 144K
Mechanical @ $200/wire	$ 72K
	$ 216K

3. Photon Detector Array #1

481 Blocks @ $1301/block	$ 626K
481 Phototubes @ $350/tube	$ 169K
481 ADC's @ $100/ADC	$ 48K
Supporting frame	$ 50K
Cables	$ 10K
	$ 903K

4. Photon Detector Array #2

200 Blocks @ $750/Block	$ 150K
200 Phototubes @ $350/tube	$ 70K
200 ADC's @ ±100/ADC	$ 20K
Supporting frame	$ 15 K
Cables	$ 5K
	$ 255K

5.	Magnet Assembly	$ 35K
6.	Transverse Drift Chamber	
	LeCroy T.D.C. 885 wires @ $50/wire = $44K	$ 44K
7.	Z Drift Chambers (Zuv)	
	Wisconsin design 2580 wires @ $70/wire =	$ 181K
8.	Time of Flight Hodoscope	
	60 elements with light division @ $1000 element	$ 60K
9.	Trigger Hodoscope	
	236 elements @ $100/element	$ 24K
	Total	$1,949K

Appendix I

Estimates of the Energy Density

We can estimate the energy density in the central region using a one dimensional model.[38] Consider a section of outgoing matter

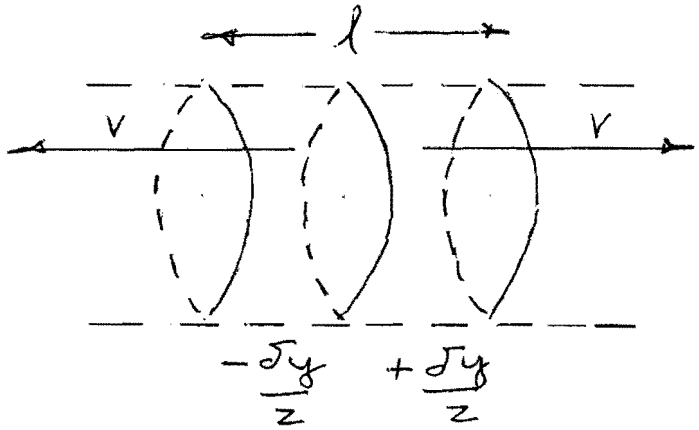

The volume of the cylinder is $A \times \ell$ where

$$\ell \simeq 2vt \simeq t\delta y \ .$$

In the non-relativistic approximation

$$2v = \delta y \ .$$

Let ε be the energy density and $A = \pi r^2$

$$\varepsilon = \frac{1}{A\times\ell}\frac{dE_A}{dt}\delta y = \frac{1}{t\pi r^2}\frac{dE_A}{dy} \ . \qquad (1)$$

t may be thought of as the lifetime of the thermalized blob. Using our experimentally determined values[27] for pp collisions at $\sqrt{s}$ = 7.7 GeV, for t and r we have

$$t = 2 \text{ fm} \quad \text{and} \quad r = 0.7 \text{ fm} \ . \qquad (2)$$

Approximating E_A by $\frac{3}{2}\bar{E}n_c$ (See Appendix II), for pions it follows that

$$\frac{dE_A}{dy} \sim (0.4 \times \frac{3}{2}) \frac{dn_c}{dy} \quad . \tag{3}$$

The 3/2 factor includes the contributions from π° mesons, the average pion energy was taken to be $\bar{E} = 0.4$ and at our energies we expect

$$\frac{dn_c}{dy} > 8 \quad . \tag{4}$$

After substituting Eqs. (2), (3) and (4) into (1), we obtain as a lower limit estimate of the available energy density at the Tevatron collider:

$$\varepsilon = \frac{0.6}{2 \times \pi(0.7)^2} \times 8 \sim \frac{1.6 \text{ GeV}}{\text{fm}^3} \quad .$$

Studying high transverse energy events Bjorken argues[39] that energy densities substantially greater than our estimates may have been already observed at the CERN $\bar{p}p$ collider.

Appendix II

The Sizes, Wire Spacings and Wire Counts of Wire Chambers

1. The Central Cylindrical Drift Chambers

Radii of cell	Wires per cell	Number of cells	Charge division	Multiple hit capability
20 to 40	16	24	yes	8

N^{W}_{total} = 384 wires Wire length = 2 meters

2. The End Cap Drift Chambers (Design II)

Radial length of wire	Wires per cell	Number of cells	Multiple hit capability
45 cm		30	4

N^{W}_{total} = 360

3. Transverse Drift Chambers (Zuv)*

Width (cm)	Wire spacing (cm)	Number of wires (3 planes)	Double hit capability
160	2	240	no
200	2	300	no
230	2	345	no

N^{W}_{total} = 885

4. Z Drift Chambers (Zuv)*

Width (cm)	Length (cm)	Wire spacing (cm)	Number of Wires (3 planes)
100	8.25	0.4	750
100	8.25	0.4	750
120	30	1.0	360
240	30	1.0	720

Total number of wires = 2580

(Zuv)* u,v are rotated by ±16° with respect to Z.

The Dimensions and Segmentation of Trigger Hodoscopes

1. The End Cap Trigger Hodoscopes (radial)

Radial length (cm) × thickness (cm)	Angular segmentation	Number	Light division
45 × 1	7.2°	50	no

Total number of hodoscope elements = 2 × 50 = 100

2. The Time of Flight Hodoscope

Hodoscope width (cm)	Cross section (cm) × (cm)	Number of segments	Light division
300	5 × 2	60	yes

Vertical element length = 1.6 meters

3. The Trigger Hodoscope on Cylindrical Chamber

Hodoscope radius (cm)	Cross section (cm) × (cm)	Number of segments	Light division
43	4 × 1	136	no

Horizontal element length = 1.0 meters

Appendix III

Parameters of the Spectrometer Magnet

The spectrometer magnet, shown in side view and end view in Fig. 22, has been designed to be as compact as possible (15") in the particle direction. Although the central field is only 3.6 kG, the unusual aspect ratio of pole width to gap height required additional steel in the regions above the coil and on the side yokes.

The mechanical parameters of the magnet are:

Yoke outer dimension, x:y:z = 15" × 45" × 82"

Gap height = 12", pole width = 5"

Coil cross section, x:y = 4" × 8"

Weight of iron = 3.9 t

Weight of 2 coils = 1.1 t

Angular acceptance: $\Delta\phi = 25°$

$\Delta\theta = \pm 35°$ ($\Delta\eta = 1.3$)

The magnet is designed to give a transverse deflection of 50 MeV/c to a particle traveling at $\theta = 90°$. The magnetic and electrical parameters corresponding to this are:

Field at gap center = 3.6 kG

Coil current density = 3.5 ka/in^2

Power dissipation = 60 kw

We estimate the total cost of the magnet to be 35K$.

Appendix IV

The Double Interaction Problem

We can simply estimate the double interaction problem. The probability of a single interaction is a collision pulse for $L = 10^{27}\ cm^{-2}\ sec^{-1}$ is

$$\frac{40/sec}{140{,}000/sec} \sim 3 \times 10^{-4} \quad .$$

The probability of a real event with multiplicity 5 n_{max} is 3×10^{-5}. We would expect an accidental double vertex background rate of $(3 \times 10^{-4})^2$ or 0.3% of the real rate. For $L = 10^{29}\ cm^{-2}\ sec^{-1}$, this would rise to 30%. However tracking through the cylindrical chambers would further reduce this by a factor of 50, (1 cm vertex uncertainty) i.e., 0.6% of the real rate.

References

1. E. Fermi, Prog. Theor. Phys. 5, 570 (1950).

2. L. D. Landau, Izv. Akad. Nouk. S.S.S.R. 17, 51 (1953); P. Carruthers and Minh-Düong Van, Phys. Rev. D 8, 859 (1973).

3. M. Gell-Mann, Synchrotron Laboratory Report CTSL-20 (1961); M. Gell-Mann, Phys. Lett. 8, 214 (1964); C. Zweig, CERN Report Nos. TH 401, 402 (1964).

4. J. D. Bjorken, Phys. Rev. 179, 1547 (1969); J. D. Bjorken and E. A. Paschos, Phys. Rev. 185, 1975 (1969); S. J. Drell, D. J. Levy and T. M. Yan, Phys. Rev. Lett. 22, 744 (1969).

5. D. Gross and F. Wilczek, Phys. Rev. Lett. 30, 1343 (1973); H. D. Politzer, Phys. Rev. Lett. 30, 1346 (1973).

6. H. Georgi and H. Politzer, Phys. Rev. D 14, 1829 (1976).

7. R. Hagedorn and J. Rafelski, Phys. Lett. 97B, 136 (1980); L. D. McLerran and B. Svetitsky, Phys. Lett. 98B, 199 (1981); J. Kuti, J. Polonyi and K. Szlachanyi, Phys. Lett. 98B, 199 (1981).

8. L. Van Hove, Phys. Lett. 118B, 138 (1982); J. D. Bjorken, Fermilab Pub. 82/44-THY.

9. J. Kogut et al., Phys. Rev. Lett. 51, 869 (1983).

10. J. Engels et al., Nucl. Phys. B205, 545 (1982).

11. UA1 Collaboration, Phys. Lett. 123B, 115 (1983); UA1 Collaboration, Phys. Lett. 107B, 320 (1981).

12. J. G. Rushbrook, Proc. of the 21st Int. Conf. on High Energy Physics C3-177.

13. UA1 Collaboration, Phys. Lett. 118B, 167 (1982).

14. J. P. Rapellin, CERN UA2 Collaboration, Proc. of the 21st Int. Conf. on High Energy Physics C3-571; M. Banner et al., Phys. Lett. 122B, 322 (1983).

15. Z. Koba, H. B. Nielsen and P. Olesen, Nucl. Phys. B40, 317 (1972).

16. S. Barshay, Phys. Rev. Lett. 49, 1609 (1982); P. Carruthers and C. C. Shih, LA-UR-83-1231; S. Krasznovszky and I. Wagner, KFKI-86-1982.

17. A. T. Laasanen et al., Phys. Rev. Lett. 38, 1 (1977).

18. J. Erwin et al., Phys. Rev. Lett. 1534, 27 (1971).

19. D. Brick et al., Nucl. Phys. B152, 45 (1979).

20. T. F. Hoang, Phys. Rev. D 8, 2315 (1973).

21. C. M. G. Lattes, Y. Fujimoto and S. Hasegawa, Phys. Rep. 65, 152 (1980).

22. F. Halzen and H. C. Liu, Phys. Rev. D 25, 1842 (1982).

23. J. D. Bjorken and H. Weisberg, Phys. Rev. D 13, 1405 (1976).

24. G. Domokos and J. L. Goldman, Phys. Rev. D 23, 203 (1981); G. Domokos, JHU-HET 8212 (1982); G. Domokos, JHU-HET 8301 (1983).

25. R. Hanbury-Brown and R. Q. Twiss, Philos. Mag. 45, 663 (1954).

26. G. I. Kopylov, Phys. Lett. 50B, 472 (1974).

27. C. Ezell et al., Phys. Rev. Lett. 38, 873 (1977).

28. K. Gottfried, Phys. Rev. Lett. 32, 957 (1974).

29. T. Akesson et al., CERN-EP/83-74.

30. W. Farr et al., Nucl. Inst. and Meth. 156, 283 (1978).

31. H. Drumm et al., Nucl. Inst. and Meth. 176, 333 (1980).

32. W. Farr et al., Nucl. Inst. and Meth. 156, 301 (1978).

33. W. Farr et al., Nucl. Inst. and Meth. 154, 175 (1978).

34. E. W. Anderson et al., Nucl. Inst. and Meth. 122, 587 (1974).

35. Kobayashi et al., KEK Internal Report 81-8.

36. T. Akesson et al., Phys. Lett. 123B, 133 (1983).

37. Private Communication, S. Snowdan.

38. J. D. Bjorken, Fermilab Pub.-82/44 THY.

39. J. D. Bjorken, Fermilab Pub.-82/59 THY.